UNIVERSITY OF OKLAHOMA

GRADUATE COLLEGE

COVERAGE ANALYSIS OF UNMANNED AERIAL VEHICLES BASED NETWORK

A THESIS

SUBMITTED TO THE GRADUATE FACULTY

in partial fulfillment of the requirements for the

Degree of

MASTER OF SCIENCE IN ELECTRICAL AND COMPUTER ENGINEERING

BY

HANEYA NAEEM QURESHI
Norman, Oklahoma
2017

COVERAGE ANALYSIS OF UNMANNED AERIAL VEHICLES BASED NETWORK

A THESIS APPROVED FOR THE
SCHOOL OF ELECTRICAL AND COMPUTER ENGINEERING

BY

Dr. Ali Imran, Chair

Dr. Kam Wai Clifford Chan

Dr. Samuel Cheng

Acknowledgments

I would like to express my sincere gratitude to my advisor, Dr. Ali Imran, for his continuous support during my M.S. study and research. His expertise, guidance, support, and patience added considerably to my graduate research experience.

I would also like to thank my fellow colleagues in BSON Lab for their support and providing a research conducive work environment.

I am extremely grateful to my family; my parents and my sister for their prayers, love and moral support.

Table of Contents

List of Figures

List of Tables

Abstract

Unmanned Aerial Vehicle (UAV) based cellular deployment research has recently gained significant attention due to its ability to overcome certain limitations of both terrestrial and satellite networks. However, most studies on the topic analyze key UAV deployment parameters, such as coverage radius and altitude while omitting or over-simplifying an important piece of UAV deployment puzzle, i.e., effect of a realistic antenna pattern. This thesis addresses the UAV deployment problem while using a realistic 3D directional antenna model and analyses the new tradeoffs between key UAV deployment parameters that emerge only when a realistic antenna model is used. The focus of this study is to identify and analyze the various UAV deployment design options after adding a new dimension of beamwidth to the UAV deployment design space. The extensive numerical results, cross validated with simulations reveal many new insights that can be crucial in practical deployments but cannot be examined with existing simplified models. Through quantitative comparison of coverage to deployment parameter sensitivity, it is shown how beamwidth may be a more feasible parameter to design optimal coverage as compared to height optimization proposed in prior literature. Moreover, the significance of optimizing both antenna beamwidth and UAV altitude in tandem with each other, rather than independently is established. Extending analysis to multiple UAVs, a hexagonal packing scheme to optimize number of UAVs needed to cover a given area is proposed. The results are compared with what was obtained by circle packing theory in prior literature. The comparison uncovers several advantages the proposed approach offers as compared to circle packing based UAV deployment.

CHAPTER 1

Introduction

1.1 Unmanned Aerial Vehicle Based Cellular Deployment

The demand for more diverse, flexible, accessible and resilient broad band service with higher capacity and coverage is on the rise. Some of these requirements can be accomplished with unmanned aerial vehicles (UAVs) acting as aerial base stations since they can overcome the limitations of both terrestrial and satellite systems. This is because of the several advantages UAV based communication offers such as higher likelihood of line-of-sight (LOS) path and less scatter without the need for ground sites as compared to terrestrial systems [1]-[3]. Moreover, the demand for increase in capacity is leading towards deployment of small cells in ground-based networks [4], resulting in the need for higher cell counts, leading to far greater ground sites. This makes the goal of attaining seamless coverage over a wide geographical area through terrestrial systems infeasible due to the limited availability of suitable sites and local regulations. This challenge is likely to aggravate with the advent of even smaller mmWave cells offering even more sporadic coverage [5].

Similarly, satellite networks have their own limitations such as high latency, high propagation loss, limited orbit space and high launching costs [6]. On the contrary, UAVs can be deployed quickly with much more flexibility to move from one point to another which is required for rapid, on-demand or emergency communications [7]-[10].

Additionally, the deployment timing is relatively less as compared to both ground based and satellite based systems as one platform and ground support is typically sufficient to start coverage. Equipment upgrades and system growth are relatively easy in UAV based systems too [11].

Fig. 1.1: UAV applications.

UAVs can thus be seen as potential enablers to meet the proliferating challenges of next generation systems in several ways. For example, they can function as complementary architectures with already existing cellular networks by acting as temporary hot spots to compensate for cell overload during peak times and emergency situations . They can also serve as stand-alone architectures to provide new infrastructure, especially in remote areas [13]. Another significant application of UAVs is in the emerging Internet of Things (IoT) technology. In this case, devices are unable to communicate over long distances due to their limited transmit power [14]. UAVs can come to the rescue by providing a means to collect the IoT data from these devices and transmitting it to their intended receivers [15]-[18]. Other applications of UAVs are shown in Fig. 1.1.

However, in order to fully reap the benefits of UAV based communication, optimal design of UAVs deployment parameters is of fundamental importance. In this thesis, UAV deployment problem is addressed by analyzing the tradeoffs between key UAV parameters such as height, antenna beamwidth, and number of UAVs while considering design

space dimensions that remain unexplored in existing studies. Leveraging a realistic system model, the analysis reveals several new UAV deployment design insights.

1.2 Previous Work and Motivation

Several studies have recently addressed UAV deployment for different service requirements, while mostly using altitude, transmission power and number of UAVs as the only three deployment parameters. For example, authors in [19] investigate the maximum coverage and optimal altitude assuming one UAV with no interference. The optimal altitude is estimated as a function of maximum allowed path loss and statistical parameters of urban environment. It is found to be the one where the derivative of radius-altitude curve becomes zero. A closed-form expression for predicting the probability of geometrical line of sight between a low altitude platform (LAP) and a ground receiver in terms of elevation angle and urban statistical parameters is derived. Based on it, the authors then estimate optimal altitude as a function of the maximum allowed path loss as well as the statistical parameters of the urban environment. The optimal altitude is found to be the one where the derivative of radius-altitude curve becomes zero. However, this work is limited to a single UAV while using mean value of shadowing (rather than its random behavior) and altitude as the only optimization parameter to control coverage.

Authors in [20] extend the work in [19] to two UAVs, with and without interference. This work addresses the deployment of drone small cells (DSCs) in terms of altitude and distance between UAVs. Based on the path loss models in [19] and [21], optimal altitude is reported in [20] for both maximum coverage and minimum required transmit power. Further, the impact of the distance between two DSCs on coverage performance is investigated. In an interference free scenario, as the length of target area increases, the optimal distance between the DSCs also increases to provide maximum coverage. In a full interference scenario, when the DSCs are close to each other, the interference between them reduces the overall coverage performance; when the DSCs are further

away from each other, interference is reduced to a minimum, but the DSCs then provide coverage mainly for areas outside the target area. It is concluded that there is an optimal distance between DSCs that provides maximum coverage.

Continuing to analyze altitude vs coverage radius relationship, in [22], the same team of authors address the deployment problem with coexistence between UAV and under laid Device-to-Device (D2D) communication networks while considering two types of users: the downlink users served by the UAV and the D2D users that communicate directly with one another. A tractable analytical framework for coverage and rate analysis is derived in this work and applied to two scenarios. The first considers a static UAV, where the average coverage probability and the system sum-rate were derived as a function of the UAV altitude and the number of D2D users. The second scenario is based on a mobile UAV in which the disk covering problem was used to find the minimum number of stop points that the UAV needed to visit in order to completely cover the area. It is reported that an optimal UAV altitude exists depending on the density of D2D users. More specifically, the optimal UAV altitude for downlink users decreases as the number of D2D users increases and the coverage radius decreases as the D2D density increases.

Another study based on UAV coexistence investigates the ways of improving grade of service with different user types in a multiple UAV system with shared coverage area and spectrum [23].

Focusing on just the altitude as a deployment parameter, [24] investigated the altitude estimation of UAVs from a more practical, real-time estimation perspective. To this end, the authors present a mixed stereoscopic vision system that consisted of a fish-eye camera and a perspective camera and then proposed a plane-sweeping algorithm to detect the ground plane and estimate the altitude. Unlike classical stereoscopic systems that are based on feature matching, their algorithm searches for the altitude that fits the homography between the two views, the calibrated sensor, and the altitude estimated by the fish-eye camera. Robustness of the method is reported, which allows for real

time estimation.

Apart from coverage area, other performance indicators are also affected by changes in UAV height, such as carrier to interference ratio and handovers. Focusing on mm-wave band, authors in [25] investigate coverage vs carrier to interference ratio patterns using an antenna pattern approximated by a cosine function raised to a power. Building upon the work in [25], the effect of lateral displacement of a UAV on interference and handovers is studied in [26]. Authors in [27] measure Receive Signal Strength Indicator (RSSI) for three UAV based cellular networks using following models: Okumura-Hata, COST-Hata, and COST Walfish-Ikegami (COST-WI). It is reported that signal strengths decrease faster with increase in altitude. However, this work considers UAVs up to an altitude of 500m because of their path loss models constraints.

Other works on UAV deployment from the perspective of optimal placement of UAVs are studied in [28]-[35]. In [28], optimal placement of low altitude platforms (LAPs) and portable base stations (PTS) is examined, particularly for disaster relief scenarios. The authors proposed an evolutionary algorithm that would find the optimal station position of both LAPs and PTS based on their radius of coverage in real time. However, the proposed scheme uses inter-cell interference coordination which would have an overhead cost that is exponential to the network size. After testing their algorithm using random scenarios and a real example from Hurricane Katrina, their results report that LAPs should represent about 20-40 of base stations in a network; more than 40 can lead to large amounts of interference, while less than 20 would require more PTS to make up for the uncovered areas. They also concluded that while PTS should be placed in the center of critical areas, LAPs should be placed on the boundaries of critical areas to mitigate interference when providing full coverage, especially in emergency situations.

By considering a constant UAV height, optimal trajectory designs are studied in [29]. Another work addressing UAV placement in disaster scenarios is [30] which proposes a dynamic algorithm that maximizes the received power by moving the LAP between

multiple points within the coverage area while also minimizing total path loss. The proposed algorithm is tested in four environments: urban, suburban, dense urban, and urban high-rise. The authors then proceed to derive an outage probability expression for each user within the system to assess the gain in both LoS and NLoS scenarios and conclude that in the case of Poisson distributed users, employment of the proposed algorithm saves more than 10dB per user.

In a more general study, [31] investigates the placement optimization of several Unmanned Aerial Base Stations (UABS). The goal in this study is to minimize the number of UABS needed to provide coverage for a group of ground terminals, where each ground terminal is in range of at least one UABS. The problem is formulated as Geometric Disk Cover (GDC) problem. To solve this problem, a polynomial-time algorithm is proposed, in which UABS are placed sequentially, starting on the perimeter of the uncovered ground terminal and moving along a spiral path towards the center until all ground terminals are covered. Each UABS is placed to cover as many ground terminals as possible. A comparison of results based on other algorithms (such optimal core-sets based algorithm [36] with exponential complexity and the low-complexity strip-based algorithm [37]) shows that this method is better that existing literature in terms of the total number of required UABS and time complexity.

Other 3-D placement models are considered [32]-[34]. Authors in [32] proposed a model that numerically computes a solution to an equivalent quadratic-constrained mixed integer non-linear optimization problem. Within this model, the altitude of the UABS and the location of both the UABS and the users in the horizontal dimension is considered. The model is tested through numerical simulations to maximize the number of covered users and results report that the size of the coverage area is affected by the environment. The model also determined the altitude and location at which the most users were covered.

Ideas introduced in [32] are further elaborated in [33] leading to the conclusion that larger

buildings require a higher UAV altitude. However, it addresses network coverage through a new Cognitive Relay Node network model in an aim to enhance the performance of standard relay nodes.

In [34], the optimal placement of unmanned aerial base stations is addressed in terms of maximum coverage and energy efficiency in a heterogeneous network context by decoupling the horizontal and vertical dimensions of the UAV placement problem. The authors of [34] propose an algorithm that maximizes the number of covered users while using minimum transmit power by considering the vertical and horizontal dimensions of the placement problem separately. The horizontal dimension is modelled as a circle placement problem and a smallest enclosing circle problem. Results report that significant power savings can be realized for highly heterogeneous scenarios and the increase in the number of covered users as the user heterogeneity increased.

Another algorithm to minimize the number of UAVs required for continuous coverage is presented in [35]. It considers the charging time, travel time, the number of subareas, and the energy capacity of each UAV. This limited energy algorithm, when compared to a straightforward method that assigned two UAVs per subarea, requires 69-94% fewer additional UAVs as the energy capacity of the UAVs is increased and only requires 67-71% fewer additional UAVs as the number of subareas increases. Specifically, when the energy capacity of the UAVs increases, the coverage time of each UAV increases but the number of additional UAVs decreases, allowing a single UAV to cover more subareas. However, as the charging time or the travel time of each UAV is increased, the number of additional UAVs needed using their approach increased.

Another aspect of the UAV deployment problem is ensuring constant connectivity along with coverage. To this end, three works are notable [38] , [39] and [40]. Authors in [38] elaborate on the topic of area coverage and connectivity by proposing a connectivity-based mobility model to maintain connectivity between the UAVs and the ground station in three scenarios: a single hop scenario, a multi hop scenario, and a campus scenario

where the UAVs surveyed an area and sent the data to a ground station. In the single hop scenario, it is revealed that coverage-based mobility spreads better as the number of UAVs increase, whereas connectivity-based mobility is not significantly influenced by the number of UAVs. In the multi hop scenario, it is observed that the connectivity of the coverage-based scheme improved almost linearly with the number of UAVs when the transmission range was sufficiently large and that there were spatial coverage improvements with the connectivity-based scheme. Hence, it is shown that there is a trade-off between achieving good coverage and maintaining connectivity, especially if there is a small number of UAVs or if the UAVs have short transmission ranges. [39] further elaborates the trade-off between coverage and connectivity using mobility models. The first mobility model proposed was a Simple Random Model where UAVs moved independently of each other without coordination. When tested, this model had poor coverage but kept up with the second model in terms of connectivity. The second model was a distributed pheromone repel model where pheromones guided the movement of the UAVs; the movement of one UAV depended on the movement of another. When tested, this model had good coverage but poor connectivity caused by the UAVs being forced away from one another. This paper shows that there is a trade-off between achieving good coverage and maintaining adequate connectivity.

Using the self-organizing network (SON) paradigm, the authors in [40] use UAVs as wireless relays to provide service for ground sensors and study the impact of number of UAVs on coverage area and connectivity. An autonomous and robust UAV network is designed and compared with a pure random walk network in realistic simulation experiments. Results validate that with the pure random walk, the connectivity continuously dropped until the whole relay network was disconnected. When replaced with the self-organizing algorithm, the connectivity converges to a high value that was maintained for the duration of the mission. Yet the work in [40] does not consider the use of UAVs as aerial base stations and their interference. Another UAV based relay network with rate optimization is studied in [41].

However, none of the aforementioned studies [19]-[41] consider the impact of antenna gain pattern on the coverage vs height trade-off. One recent study [42] that does consider the effect of antenna uses a step-wise antenna gain model with only two possible values of antenna gain. Analysis incorporating realistic antenna model has become more important since several studies are already considering implementations of directional antenna in UAV-based cellular systems [43], such as smart WiFi directional antennas with servo motors [44]. While the UAV deployment problem has been investigated in a large number of recent studies as discussed above, to the best of author's knowledge, this is the first work to study the optimization of UAV deployment design parameters while using a realistic 3D directional antenna model in the system. The analysis presented in this thesis shows that the use of a realistic antenna pattern makes a trend shifting difference in the height vs coverage trade-off and adding a new dimension of beamwidth to the UAV deployment design space that remains unexamined in earlier studies.

1.3 Research Objectives

While the UAV deployment problem has been investigated in several recent studies as discussed in Section 1.2, investigation of the interplay between key optimization parameters affecting the UAV deployment problem while using a realistic 3D directional antenna model in the system has not yet been covered. Hence, the focus of this study is to identify several UAV deployment design options while incorporating a realistic model for a practical directional antenna. The research objective is to uncover how the key UAV deployment parameters change after adding a new dimension of beamwidth to the UAV deployment design space and then to present several new insights from a system design perspective based on the analysis.

1.4 Contributions

The contributions of this thesis can be summarized as follows:

- A mathematical framework for UAV deployment is proposed by incorporating the effect of a practical directional antenna. Current studies on UAV deployment either ignore the effect of 3D directional antenna [19]-[40] or consider an over-simplified model for antenna gain [42]. Therefore, UAV deployment analysis presented in these studies, yields results on optimal height, coverage radius and number of UAVs that may not hold for real UAV deployments. This is addressed by using 3GPP defined 3D parabolic antenna pattern whose gain is realistically dependent on not only beamwidth but also three dimensional elevation angle.

- Analytical expressions for coverage characterized by received signal strength (RSS) as a function of height, beamwidth and coverage radius are derived.

- Prior works omit either one or more aspects in the modelling of UAV coverage that affect tradeoffs between key UAV deployment objectives and parameters [19]-[42], thus providing representation of optimal UAV deployment that may be far from reality. This thesis holistically investigates practical UAV deployment by quantitatively analyzing tradeoffs between following parameters: (i) radius with beamwidth for varying heights, (ii) radius with height for different beamwidths and (iii) beamwidth with height for different coverage radii. To the author's best knowledge, the analysis presented in this thesis for the first time quantifies the interplay between five factors that determine UAV based coverage: angular distance dependent antenna gain, elevation angle dependent probability of line of sight, shadowing, free space path loss (FSPL) and height.

- The analysis is extended for varying frequencies and environments and derived expressions for probability density function (PDF) of RSS are also corroborated through simulations and analysis.

- Some works on UAV deployment [19], [42] propose UAV altitude as the only optimization parameter to control coverage. Such height optimization based deployment solutions overlook the fact that UAV heights, unlike terrestrial base station heights, are dictated by several factors beyond the system designer's control, such as technical limitations on altitude imposed by earth's atmospheric layers and regulatory constraints imposed by aviation authorities. However, based on the analysis of the effect of beamwidth and altitude on coverage, it is shown in this work that:
  - There exists an optimal beamwidth for given height for maximum coverage radius and vice versa. An expression is also derived that allows to determine the optimal beamwidth/height for desired coverage radius.
  - Antenna beamwidth is a more practical design parameter to control coverage instead of UAV altitude. This is done by quantifying the sensitivity of coverage to both height and beamwidth and drawing a comparison between the two.
  - Contrary to what has been assumed implicitly or explicitly in prior studies, UAV altitude can not be optimized independent of antenna beamwidth. In fact, both parameters need to be optimized in tandem with each other for realistic deployment.
- This work also extends the analysis to multiple UAVs. Some recent studies have leveraged circle packing theory to determine the number of UAVs needed to cover a given area [42]. However, this approach has two caveats: 1) It leaves significant coverage holes when two or more UAVs are used to cover an area. 2) The number of UAV increase dramatically with increase in required coverage probability. To circumvent the problems posed by circle packing theory, use of hexagonal packing is proposed and results are compared with that obtained by circle packing to identify several further advantages hexagonal packing offers.

- Continuing analysis on multiple UAVs, optimal beamwidth for different number of UAVs that yields maximum total coverage for a target geographical area is determined. The results are useful from a system design perspective since the trend of beamwidth with minimum number of UAVs needed to achieve desired coverage opens up new design options for wireless system design. More specifically, it is shown how it is possible to accomplish the same coverage requirements with less infrastructure (number of UAVs) from the proposed model by controlling beamwidth. This is of fundamental importance since when deploying an aerial network, it is important to properly estimate the infrastructure required to meet desired system requirements, especially because radio resource and energy are quite limited in such networks [45], [46].

1.5 Articles Currently Under Review for Publication

1. H. N. Qureshi and A. Imran, "New Insights into UAVs Coverage Tradeoffs using a Practical Antenna Model: What Model Simplifications Must be Avoided?," in IEEE Antennas and Wireless Propagation Letters (submitted October 2017)

2. H. N. Qureshi and A. Imran, "On the Tradeoffs between Coverage Radius, Altitude and Beamwidth for Practical UAV Deployments," in IEEE Transactions on Aerospace and Electronics Systems (to be submitted November 2017)

1.6 Organization

The rest of this thesis is organized as follows: Chapter 2 presents the system model for UAV based cellular deployment. This covers all aspects of the system model, such as antenna gain pattern, free space path loss, shadowing, probability of line-of-sight and non-line-of-sight links and other environment-dependent variabilities. In Chapter 3, the system model is further developed and mathematical framework for the proposed model

is formulated. This includes optimization problems based on coverage probabilities and received signal strength (RSS). Probability density functions (PDF) of RSS, both at any arbitrary point as well as inside a certain geographical area are also derived in this chapter. A comprehensive analysis of tradeoffs between coverage radius, UAV height and beamwidth is presented in Chapter 4. Chapter 5 extends the analysis to varying frequencies and environments and presents several new insights revealed by the analysis. The impact of UAV design space dimensions on RSS is investigated in Chapter 6. In Chapter 7, a comparison is done between two different parameters (height and beamwidth) used to control coverage. Chapter 8 extends the analysis to multiple UAVs. In this chapter, a hexagonal packing strategy is proposed for multiple UAVs and results are compared with circle packing strategy proposed in prior work. Finally, conclusions and discussions with regard to future work are given in Chapter 9.

CHAPTER 2

System Model for UAV based Cellular Deployment

The system model illustrated in Fig. 2.1 is considered. The UAV resides at a height h in the center of a cell with coverage radius r. In Fig. 2.1, ϕ_{tilt} is the tilt angle in degrees of the antenna mounted on UAV, ϕ_{MS} is the vertical angle in degrees from the reference axis (for tilt) to the mobile station (MS). θ_a, in degrees, is the angle of azimuth orientation of the antenna with respect to horizontal reference axis i.e., positive x-axis and θ_{MS}, in degrees, is the angular distance of MS from the horizontal reference axis.

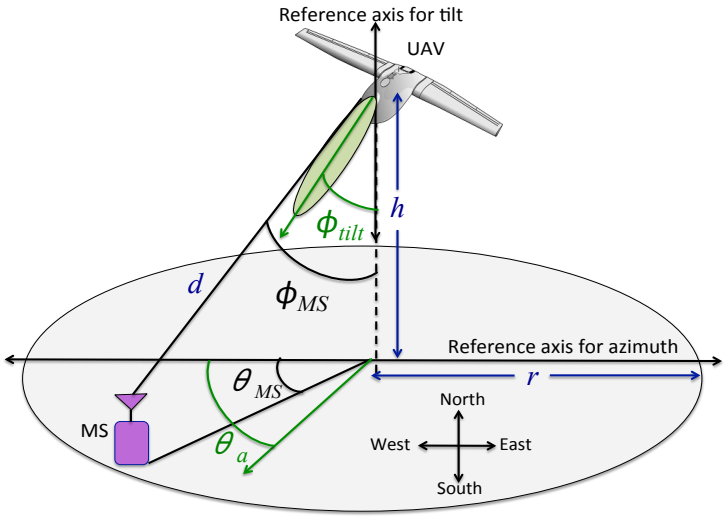

Fig. 2.1: System model.

Utilizing the geometry in Fig. 2.1, the perceived antenna gain from the UAV using a three dimensional antenna model recommended by 3GPP [47], at the location of MS can be represented as in (2.1), where B_{EW} and B_{NS} represent the beamwidths (in degrees) of

$$G(\phi_{MS}, B_{NS}, B_{EW}) = \lambda_{NS}\left(G_{\max} - \min\left(12\left(\frac{\phi_{MS}-\phi_{tilt}}{B_{NS}}\right)^2, A_{\max}\right)\right) + \lambda_{EW}\left(G_{\max} - \min\left(12\left(\frac{\theta_{MS}-\theta_a}{B_{EW}}\right)^2, A_{\max}\right)\right) \tag{2.1}$$

the UAV antenna in East-West and North-South directions respectively while λ_{EW} and λ_{NS} represent the weighting factors for the beam pattern in both directions respectively. They are unit less variables and equal to 0.5 in this study. G_{max} and A_{max} denote the maximum antenna gain in dB at the bore sight of the antenna and maximum antenna attenuation at the sides and back of bore sight respectively.

The air-to-ground channel can be characterized in terms of line-of-sight (LoS) and non-line-of-sight (NLoS) links between the UAV and MS. Prior studies have used channel models proposed in [21], [48]-[50]. The channel models proposed in [48] and [49] are suited to only dense urban and typical European cities respectively. Moreover, channel models presented in [21], [48]-[49] lack measurement based validation. On the other hand, the channel model in [50] not only provides a simulation based data for a diverse range of elevation angles, environments and frequencies, but also has been validated through extensive empirical measurements. Hence, the UAV channel model proposed in [50] is used to estimate the probability of LoS link as follows:

$$P_l(\phi_{MS}) = 0.01j - \frac{0.01(j-k)}{1 + (\frac{90-\phi_{MS}-l}{m})^n} \tag{2.2}$$

where $(j, ...n)$ are the set of empirical parameters for different types of environments and are given in Table 2.1. The angle, $90 - \phi_{MS} = \tan^{-1}(\frac{h}{r})$ is the angle of elevation of the MS to the UAV in degrees. The probability of NLoS link is then $1 - P_l(\phi_{MS})$.

In addition to free space path loss, UAV-MS signal faces an elevation angle dependent shadowing with the following mean and standard deviation [50]:

$$\mu_{sh}, \sigma_{sh} = \frac{p_v + (90 - \phi_{MS})}{q_v + t_v(90 - \phi_{MS})} \tag{2.3}$$

where p_v, q_v and t_v are parameters obtained from empirical measurements given in Table 2.2 and the subscript $v = \{\mu, \sigma\}$, is used to indicate that the parameters are for mean and standard deviation, respectively

The received signal strength (RSS) in LoS and NLoS links, as a function of path loss

Table 2.1: Environment dependent parameters for line-of-sight probability.

	Suburban	Urban	Dense urban	High rise urban
j	101.6	120.0	187.3	352.0
k	0	0	0	-1.37
l	0	0	0	-53
m	3.25	24.30	82.10	173.80
n	1.241	1.229	1.478	4.670

Table 2.2: Environment dependent parameters for shadowing.

f (GHz)		p_v	q_v	t_v
2.0	$v=\mu$	-94.20	-3.44	0.0318
	$v=\sigma$	-89.55	-8.87	0.0927
3.5	$v=\mu$	-92.90	-3.14	0.0302
	$v=\sigma$	-89.06	-8.63	0.0921
5.5	$v=\mu$	-92.80	-2.96	0.0285
	$v=\sigma$	-89.54	-8.47	0.9000

and antenna gain can now be represented as:

$$R_l(h, r, B_{NS}, B_{EW}) = T + G - 20 \log \left(\frac{4\pi f d}{c} \right) - X_l \tag{2.4}$$

$$R_n(h, r, B_{NS}, B_{EW}) = T + G - 20 \log \left(\frac{4\pi f d}{c} \right) - X_n - X_s \tag{2.5}$$

where T is transmitted power and X_s is shadow fading Gaussian $\mathcal{N}(\mu_{sh}, \sigma_{sh})$ random variable (RV) with mean μ_{sh} and standard deviation σ_{sh}. For realistic system level modeling of mobile systems, random components in dB, X_l and X_n are added as environment dependent variables utilizing the log-normal distribution with a zero mean [50]. X_l and X_n are therefore, $\mathcal{N}(0, \sigma_l)$ and $\mathcal{N}(0, \sigma_n)$ RVs, where σ_l and σ_n denote the standard deviations of LoS and NLoS links respectively. G is a function of $\phi_{MS}(h, r), B_{NS}$ and B_{EW} given by (2.1).

CHAPTER 3

Mathematical Framework for Proposed System Model

3.1 Coverage Probability

The UAV coverage area is defined as a set of points in circle of radius r, where a MS experiences a RSS, S_r above a threshold, γ. Here, r is measured from the projection of UAV on ground. Then, the RSS at the boundary exceeds a certain threshold, $\gamma = T - PL_{max}$ with a probability, $P_{cov} \geq \epsilon$, where PL_{max} is the maximum allowable path loss. We define this coverage probability, P_{cov} as:

$$P_{cov} = \mathrm{P}[S_r \geq \gamma] = P_l(\phi_{MS})\mathrm{P}[R_l(h, r, B_{NS}, B_{EW}) \geq \gamma] + P_n(\phi_{MS})\mathrm{P}[R_n(h, r, B_{NS}, B_{EW}) \geq \gamma] \tag{3.1}$$

First, $\mathrm{P}[R_n(h, r, B_{NS}, B_{EW}) \geq \gamma]$ is calculated using (2.5) as in (3.2)-(3.4), where (3.4) is a result of complementary cumulative distribution function of a Gaussian random variable and substituting $\gamma = T - PL_{max}$ in (3.3) and $G(\phi_{MS}, B_{NS}, B_{EW})$ is defined in (2.1). Without loss of generality, it is assumed that X_n and X_s are independent RVs and thus $X'_n = X_n + X_s$ with mean $\mu'_n = \mu_{sh}$ and standard deviation, $\sigma'_n = \sqrt{\sigma_{sh}^2 + \sigma_n^2}$.

$$\mathrm{P}\left[R_n\left(h, r, B_{NS}, B_{EW}\right) \geq \gamma\right] = \mathrm{P}\left[T + G(\phi_{MS}, B_{NS}, B_{EW}) - 20\log\Big(\frac{4\pi f d}{c}\Big) - X_n - X_s \geq \gamma\right] \tag{3.2}$$

$$= \int_{\gamma}^{\infty} \frac{1}{\sqrt{2\pi}\sigma'_n} \exp\left[-\frac{1}{2}\left(\frac{X'_n - \left(T + G(\phi_{MS}, B_{NS}, B_{EW}) - 20\log\left(\frac{4\pi f d}{c}\right) - \mu'_n\right)}{\sigma'_n}\right)^2\right] dX'_n \tag{3.3}$$

$$= Q\left(\frac{20\log\left(\frac{4\pi f d}{c}\right) + \mu_{sh} - G(\phi_{MS}, B_{NS}, B_{EW}) - PL_{max}}{\sqrt{\sigma_{sh}^2 + \sigma_n^2}}\right) \tag{3.4}$$

Similarly, $\mathrm{P}[R_l(h, r, B_{NS}, B_{EW}) \geq \gamma]$ is computed, which yields the following expression in (3.5):

$$\mathrm{P}\left[R_l\left(h, r, B_{NS}, B_{EW}\right) \geq \gamma\right] = Q\left(\frac{20\log\left(\frac{4\pi fd}{c}\right) - G(\phi_{MS}, B_{NS}, B_{EW}) - PL_{max}}{\sigma_l}\right) \quad (3.5)$$

where $Q(z) = \frac{1}{\sqrt{2\pi}} \int_z^\infty \exp(\frac{-u^2}{2})\, du$.

Moreover, from cell geometry in Fig. 2.1 (under the assumption: height of MS $<<$ h), ϕ_{MS} and d can be expressed as:

$$\phi_{MS} = \tan^{-1}\left(\frac{r}{h}\right), \quad d = \sqrt{h^2 + r^2} \quad (3.6)$$

For sake of simplicity of expression, it is assumed that the antenna beamwidth in EW and NS direction is symmetric i.e., $B_{EW} = B_{NS} = B$ in (2.1). We assume $\theta_a = 0$ and $\theta_{MS} = \phi_{MS}$ as tampering with the tilt direction is beyond the scope of this study and can be considered in future studies. Further, G_{max} can be approximated as $10\log\left(\frac{29000}{B^2}\right)$ [51] and A_{max} can be ignored without impacting the required accuracy of this antenna model that mainly concerns gain on and around the bore site. Applying these simplifications to (2.1), substituting (2.1) and (3.6) in (3.4)-(3.5) and then making use of (3.1) yields the expression for P_{cov} in (3.7). Note that the radius, r can also be translated into the position of MS on ground by: $r = \sqrt{x^2 + y^2}$, where x and y represent Cartesian coordinates for the location of user on ground.

$$P_{cov}(r, h, B) = \left(0.01j - \frac{0.01(j-k)}{1 + \left(\frac{\tan^{-1}\left(\frac{h}{r}\right) - l}{m}\right)^n}\right) Q\left(\frac{20\log\left(\frac{4\pi f\sqrt{h^2+r^2}}{c}\right) - 10\log\left(\frac{29000}{B^2}\right) + 12\left(\frac{\tan^{-1}\left(\frac{r}{h}\right) - \phi_{tilt}}{B}\right)^2 - PL_{max}}{\sigma_l}\right) +$$

$$\left(1 - 0.01j + \frac{0.01(j-k)}{1 + \left(\frac{\tan^{-1}\left(\frac{h}{r}\right) - l}{m}\right)^n}\right) Q\left(\frac{20\log\left(\frac{4\pi f\sqrt{h^2+r^2}}{c}\right) + \mu_{sh} - 10\log\left(\frac{29000}{B^2}\right) + 12\left(\frac{\tan^{-1}\left(\frac{r}{h}\right) - \phi_{tilt}}{B}\right)^2 - PL_{max}}{\sqrt{\sigma_{sh}^2 + \sigma_n^2}}\right) \quad (3.7)$$

3.1.1 Optimization Problem for Maximum Coverage Radius

In order to find the maximum cell radius (r^*), this study finds the largest r for which received signal (R) at the boundary exceeds a certain threshold, $\gamma = T - PL_{max}$ with a probability, $P_{cov} \geq \epsilon$. The optimization problem can thus be written as:

$$r^* = \max\{r|\mathrm{P}[R \geq \gamma] \geq \epsilon\} \quad = \{r|\big(P_l\,(\phi_{MS})\mathrm{P}[R_l(h, r, B_{NS}, B_{EW}) \geq \gamma] + P_n(\phi_{MS})\mathrm{P}[R_n(h, r, B_{NS}, B_{EW}) \geq \gamma]\big) \geq \epsilon\} \quad (3.8)$$

Using the probability of coverage expression derived in (3.7), the optimization problem in 3.8 along with constraints can be represented as:

$$r^* = \max_{h,B} r$$

$$\text{s.t.} \quad \left[\left(0.01a - \frac{0.01(a-b)}{1+\left(\frac{\tan^{-1}\left(\frac{h}{r}\right)-k}{l}\right)^m}\right)Q\left(\frac{20\log\left(\frac{4\pi f\sqrt{h^2+r^2}}{c}\right) - 10\log\left(\frac{29000}{B^2}\right) + 12\left(\frac{\tan^{-1}\left(\frac{r}{h}\right)-\phi_{tilt}}{B}\right)^2 - PL_{max}}{\sigma_l}\right) + \left(1 - 0.01a + \frac{0.01(a-b)}{1+\left(\frac{\tan^{-1}\left(\frac{h}{r}\right)-k}{l}\right)^m}\right)Q\left(\frac{20\log\left(\frac{4\pi f\sqrt{h^2+r^2}}{c}\right) + \mu_s - 10\log\left(\frac{29000}{B^2}\right) + 12\left(\frac{\tan^{-1}\left(\frac{r}{h}\right)-\phi_{tilt}}{B}\right)^2 - PL_{max}}{\sqrt{\sigma_s^2+\sigma_n^2}}\right)\right] \geq \epsilon$$

$$0 < B < 180, \quad 0 < h < 10,000 \quad (3.9)$$

3.2 Received Signal Strength

3.2.1 RSS at any arbitrary location in cell

One way to investigate the received signal strength (RSS) on ground is by evaluating the expected value of S_r as follows:

$$
\begin{aligned}
\mathbf{E}[S_r] &\overset{(k)}{=} P_l\,\mathbf{E}[S_r|\text{LoS}] + P_n\,\mathbf{E}[S_r|\text{NLoS}] \\
&= P_l\,\mathbf{E}[R_l - R_n] + \mathbf{E}[R_n] \\
&= \left(0.01j - 1 - \frac{0.01(j-k)}{1+\left(\frac{\tan^{-1}(\frac{h}{r})-l}{m}\right)^n}\right)\mu_{sh} - 20\log\left(\frac{4\pi f d}{c}\right) \\
&\qquad + T - 12\left(\frac{\tan^{-1}\left(\frac{r}{h}\right)-\phi_{tilt}}{B}\right)^2 + 10\log\left(\frac{29000}{B^2}\right) \qquad (3.10)
\end{aligned}
$$

where (k) is a result of the law of total expectation and P_l, R_l and R_n are functions of r, h and B and defined in (2.2), (2.4) and (2.5) respectively.

However, S_l and S_n are random variables due to shadowing, therefore, RSS will also be a random variable. If one realization of this random variable at any particular cell location (determined by r) is considered, then for a UAV deployed at a certain height and beamwidth, one realization of RSS can be expressed as:

$$
S_{i,r} = P_l R_{l,i} + P_n R_{n,i} \qquad (3.11)
$$

where the subscript, i, r, denotes i-th realization of the random variables at any arbitrary radius, r . By considering several such realizations at a particular value of r, h and B, RSS can also be modelled as a Gaussian random variable with a certain mean, μ_s and variance, σ_s^2 given by (3.10) and (3.12) respectively.

$$
\sigma_s^2 = \left(0.01j - \frac{0.01(j-k)}{1+\left(\frac{tan^{-1}(\frac{h}{r})-l}{m}\right)^n}\right)^2 \sigma_l^2 + \left(1 - 0.01j + \frac{0.01(j-k)}{1+\left(\frac{tan^{-1}(\frac{h}{r})-l}{m}\right)^n}\right)^2 (\sigma_n^2 + \sigma_{sh}^2) \qquad (3.12)
$$

In order to derive an analytical expression for the probability distribution function (PDF) of random variable, S_r, (3.11) is rewritten in terms of two other random variables, S_l and S_n, where $S_l = P_l R_l$ and $S_n = P_n R_n$. Then, from (3.11), the random variable, received signal strength at any point within the cell can be expressed as:

$$S_r = S_l + S_n \tag{3.13}$$

It is worth noting that S_l and S_n are independent random variables since X_l and X'_n are independent. Hence, in order to derive an analytical expression for S_r, the following theorem from Grinstead and Snell [52] is utilized:

Theorem 1 *Let X and Y be two independent random variables with density functions $f_X(x)$ and $f_Y(y)$. Then the sum $Z = X + Y$ is a random variable with density function $f_Z(z)$, where f_Z is the convolution of f_X and f_Y:*

$$f_Z(z) = (f_Y * f_X)(z) = \int_{-\infty}^{\infty} f_Y(z-x) f_X(x) dx \tag{3.14}$$

The PDF of S_r, by making use of Theorem 1 along with applying some transformations of random variables yields the expression in (3.15).

$$f_{S_r}(s_r) = \frac{\exp\left[\frac{-\left[s_r - \left(1-0.01j+\frac{0.01(j-k)}{1+\left(\frac{\tan^{-1}(h/r)-l}{m}\right)^n}\right)\left(\frac{p_\mu+\tan^{-1}(h/r)}{q_\mu+t_\mu\tan^{-1}(h/r)}\right)-T+20\log\left(\frac{4\pi f\left(\sqrt{h^2+r^2}\right)}{c}\right)-10\log\left(\frac{29000}{B^2}\right)+12\left(\frac{\tan^{-1}(r/h)}{B}\right)^2\right]^2}{2\sigma_l^2\left(\frac{0.01(j-k)}{1+\left(\frac{\tan^{-1}(h/r)-l}{m}\right)^n}\right)^2+\left(1-\frac{0.01(j-k)}{1+\left(\frac{\tan^{-1}(h/r)-l}{m}\right)^n}\right)^2\left(\sigma_n^2+\left(\frac{p_\sigma+\tan^{-1}(h/r)}{q_\sigma+t_\sigma\tan^{-1}(h/r)}\right)^2\right)}\right]}{\sqrt{2\pi\sigma_l^2\left(\frac{0.01(j-k)}{1+\left(\frac{\tan^{-1}\left(\frac{h}{r}\right)-l}{m}\right)^n}\right)^2+\left(1-\frac{0.01(j-k)}{1+\left(\frac{\tan^{-1}\left(\frac{h}{r}\right)-l}{m}\right)^n}\right)^2\left(\sigma_n^2+\left(\frac{p_\sigma+\tan^{-1}\left(\frac{h}{r}\right)}{q_\sigma+t_\sigma\tan^{-1}\left(\frac{h}{r}\right)}\right)^2\right)}} \tag{3.15}$$

Proof 1 *Derivation of* (3.15) *is provided in Appendix.*

3.2.2 RSS inside a geographical region

The normalized PDF of received signal strength inside a geographical region (denoted by S) by assuming that the UAV resides at coordinates (x,y,z) = (0,0,h) where h is height of UAV, can then be found as follows:

$$f_S(s) = \frac{1}{A} \iint_A f_{S_r}(s, x, y) dx dy \tag{3.16}$$

in some geographical region A that lies in the xy-plane. The integral in (3.16) can be solved through numerical methods, for example, it can be approximated by discretizing the function in (3.15) as follows:

$$\begin{aligned} f_S(s) &= \frac{1}{x_t y_t} \int_{-x_t}^{x_t} \int_{-y_t}^{y_t} f_{S_r}(s_r) dy dx \\ &\simeq \frac{1}{M_x M_y \Delta x \Delta y} \sum_{j=-M_x}^{M_x} \sum_{i=-M_y}^{M_y} f[s_{r,i}]_j \Delta y \Delta x \end{aligned} \tag{3.17}$$

where $f[s_{r,i}]$ is a discrete sequence $\{f[s_{r,i}] : i \in \{-M_y, \Delta y, 2\Delta y, ...M_y\}\ \}$ obtained by evaluating $f_{S_r}(s_r)$ in (3.15) at $2M_y$ equally spaced discrete points from $-y_t$ to y_t, with a separation interval given by $\Delta y = y_t/M_y$. Similarly, $\{f[s_{r,i}]_j : j \in \{-M_x, \Delta x, 2\Delta x, ...M_x\}\ \}$ is obtained by evaluating $f[s_{r,i}]$ at $2M_x$ equally spaced discrete points from $-x_t$ to x_t, with a separation interval given by $\Delta x = x_t/M_x$. This approach yields a fairly close approximation for $\Delta x = \Delta y = 1$.

CHAPTER 4

Tradeoffs between Coverage Radius, Beamwidth and Height

The formulation in (3.9) is a nonlinear multi-variable optimization problem. Furthermore, (3.7) is an implicit equation in r, i.e, r cannot be expressed explicitly in terms of h, B_{NS} and B_{EW}. However, thanks to the easily evaluable form of (3.9) and small search space, we can solve (3.9) even via brute force. A 3D plot of coverage radius (r) as a function of height (h) and beamwidth (B) for $PL_{max} = 120$ dB, $\phi_{tilt} = 0^o$, $\epsilon = 0.8$ and $f = 2$ GHz is depicted in Fig. 4.1 for a suburban environment.

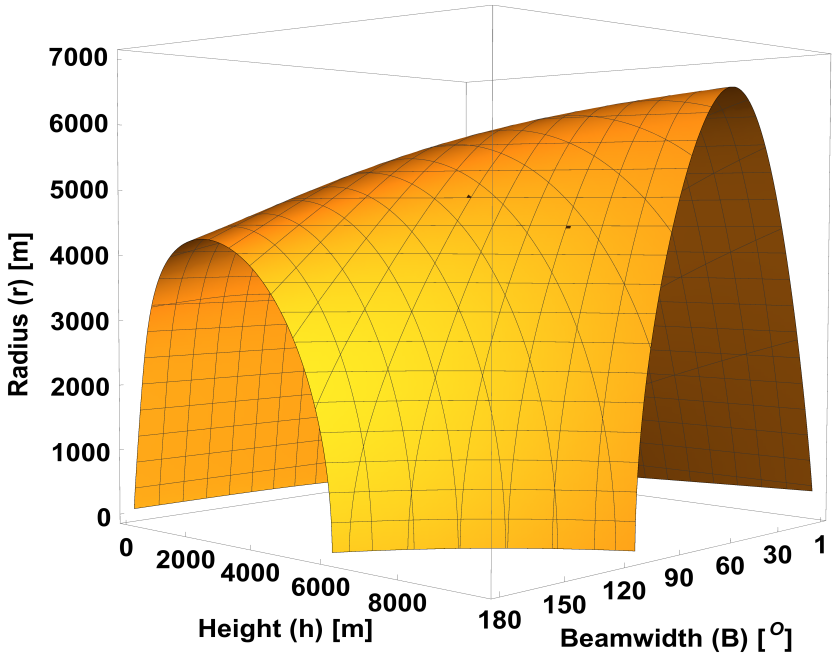

Fig. 4.1: Coverage radius with varying height and beamwidth.

It can be observed from Fig. 4.1 that initially, as the height of the UAV increases for a given beamwidth, the coverage radius also increases. However, as beamwidth increases, coverage radius increases with increase in height, reaches an optimal point and then starts to decrease. This is a new insight compared to earlier studies with simplistic antenna models [42]. Similarly, for most of the range of height, coverage radius does

not increase monotonically with beamwidth. This trend is also in contrast to results in prior studies [20] [22] [28] [40], [42].

Before analyzing these tradeoffs in detail, the behaviour of mean RSS with varying heights, beamwidths and coverage radius is presented. Then, these behaviours are analyzed in detail by providing a comprehensive analysis of the tradeoffs between height, radius and beamwidth in different environment and frequency scenarios.

Fig. 4.2 and Fig. 4.4 illustrate how the mean RSS varies with beamwidth and height with increasing cell radius r. The scenario in Fig. 4.2 consists of a UAV deployed at a height of 3500m in a suburban environment at $f = 2$GHz, $P_t = 40$dBm and $\phi_{tilt} = 0^o$. Since a narrow beamwidth can only cover a small coverage area, the decrease in RSS with increasing radius is very rapid at low beamwidths. The trend of RSS with beamwidth is more clearly depicted in Fig. 4.3(a)-4.3(c), which are zoomed-in plots of Fig. 4.2 for $20 \leq B < 180$. The mean RSS decreases with beamwidth for r upto 800m approximately (Fig. 4.3(a)). As r increases further, this trend starts to reverse and cell radius initially increases, reaches to a maximum point and then decreases (Fig. 4.3(b)). From $r > 2500$m, this trend reverses completely and RSS increases with increasing beamwidth (Fig. 4.3(c)). Note however, that the maximum RSS is still at small beamwidths and small radii.

In Fig. 4.4, mean RSS is plotted for $B = 50^o$. As expected, RSS decreases as r increases for any fixed height. However, for any r, RSS initially increases with height, reaches to a peak value and then decreases as height increases further.

These curves quantify the interplay that exists between factors that impact the coverage of UAV simultaneously: angular distance dependent realistic non-linear antenna gain model, elevation angle dependent probability of line of sight, shadowing, and a measurement backed path loss. Most prior studies on UAV coverage [19]-[42] omit one or more of these factors. A comprehensive analysis of these factors, and comparison of new trends revealed by the analysis with the results in prior literature, where pertinent

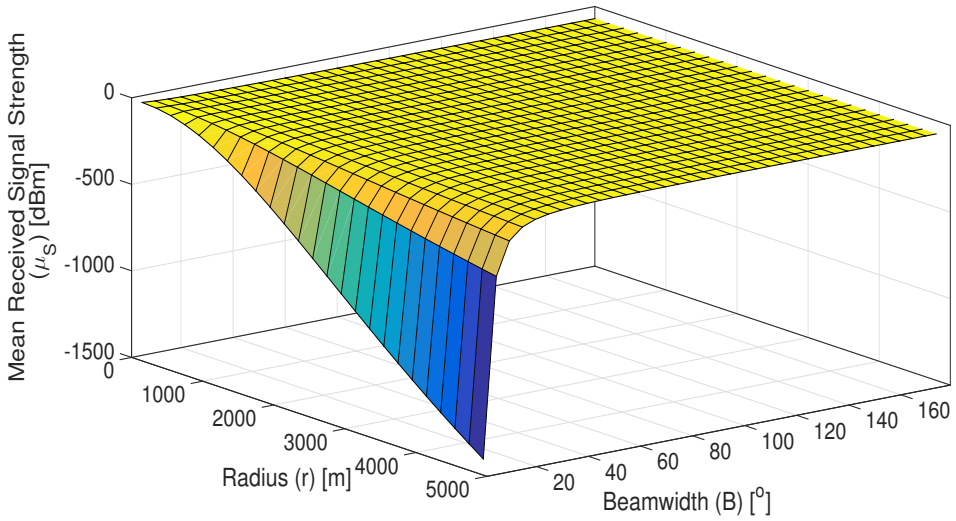

Fig. 4.2: Mean received signal with varying beamwidth at $h = 3500$m.

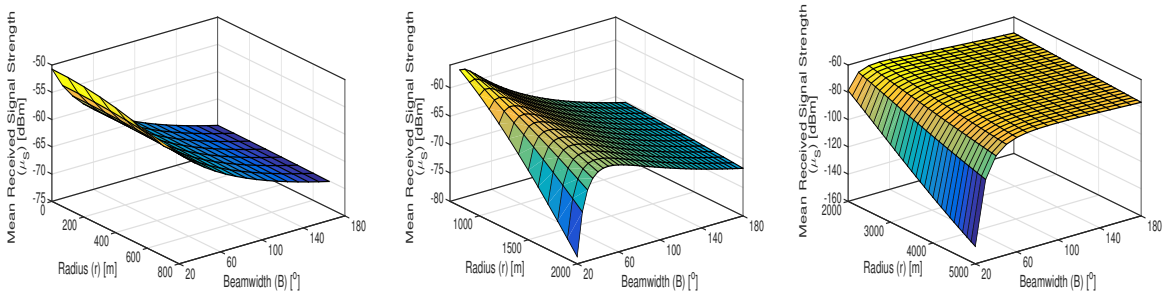

(a) 0m$< r <$ 800m (b) 800m$< r <$ 2000m (c) 2000m$< r <$ 5000m

Fig. 4.3: Mean received signal on ground with varying beamwidths $> 20^o$

is presented next.

4.1 Coverage Radius vs Beamwidth

Fig. 4.5 shows coverage radius verses beamwidth plotted by utilizing (3.7) for $PL_{max} =$ 115dB, $\phi_{tilt} = 0^o$, $\epsilon = 0.8$ and $f = 2$ GHz in a suburban environment for different heights. As the height of UAV increases, ϕ_{MS} in (3.6) decreases (angle of elevation increases), leading to an increase in probability of LoS link in (2.2), decrease in shadowing in (2.3) and increase in free space path loss (as d increases).

While the effect of these factors on coverage has been studied in earlier studies [19]-[41],

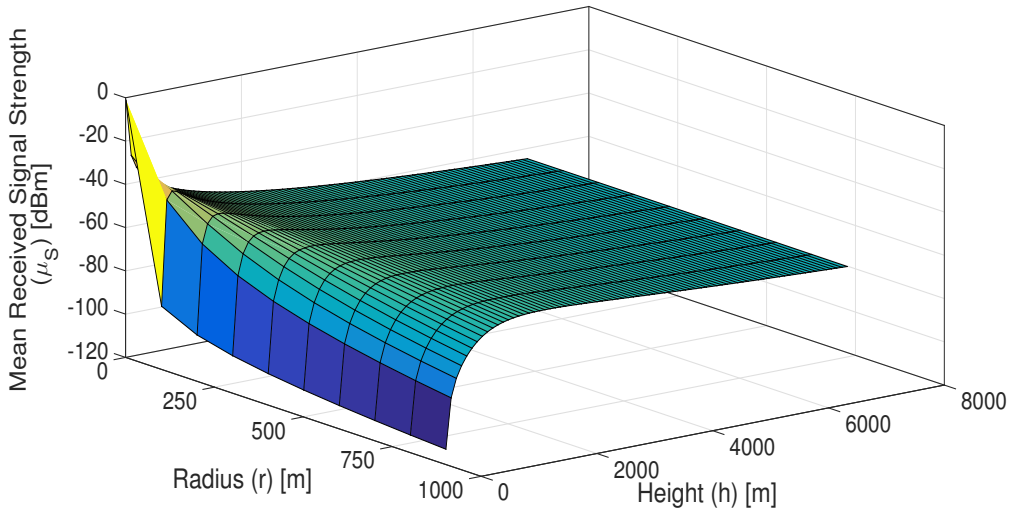

Fig. 4.4: Mean received signal with varying height for $B = 50^o$.

the impact of the fourth factor, antenna gain in conjunction with these three factors remained unexamined. Fig. 4.6 shows that impact of this fourth factor is so profound that at a given cell radius, it results in a height (h'), after which the antenna gain trend with increasing beamwidth reverses. The larger antenna gain at a given r is observed with increased height because, for the same MS location, ϕ_{MS} in (3.6) decreases. For any two beamwidths, B_1 and B_2, h' is the point of intersection of gain verses height graphs illustrated in Fig. 4.6 for $r = 5000$m. h' can be calculated as follows:

$$10\log\left(\frac{29000}{B_1^2}\right) - 12\left(\frac{\tan^{-1}\left(\frac{r}{h'}\right)}{B_1}\right)^2 = 10\log\left(\frac{29000}{B_2^2}\right) - 12\left(\frac{\tan^{-1}\left(\frac{r}{h'}\right)}{B_2}\right)^2$$

$$h' = r\left(\tan\sqrt{\frac{5}{3}\log\left(\frac{B_2}{B_1}\right)\left(\frac{B_1^2 B_2^2}{B_2^2 - B_1^2}\right)}\right)^{-1} \tag{4.1}$$

The trend shift in Fig. 4.5 in light of the aforementioned factors can then be explained as follows: as height increases up to 1000m, the increase in antenna gain and decrease in shadowing offsets the increased free space path loss. As height increases beyond 1000m, the increase in antenna gain and decrease in shadowing is overshadowed by the increase in free space loss. As a result, the coverage radius increases with beamwidth, approaches to a maximum value and then starts to decrease. Our analysis quantifies this maximum

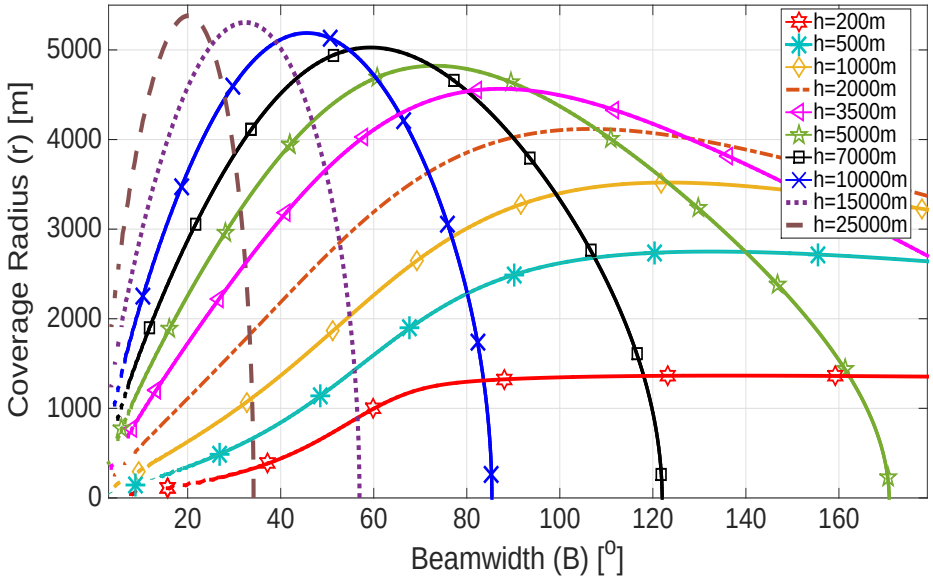

Fig. 4.5: Coverage radius against beamwidth for different heights.

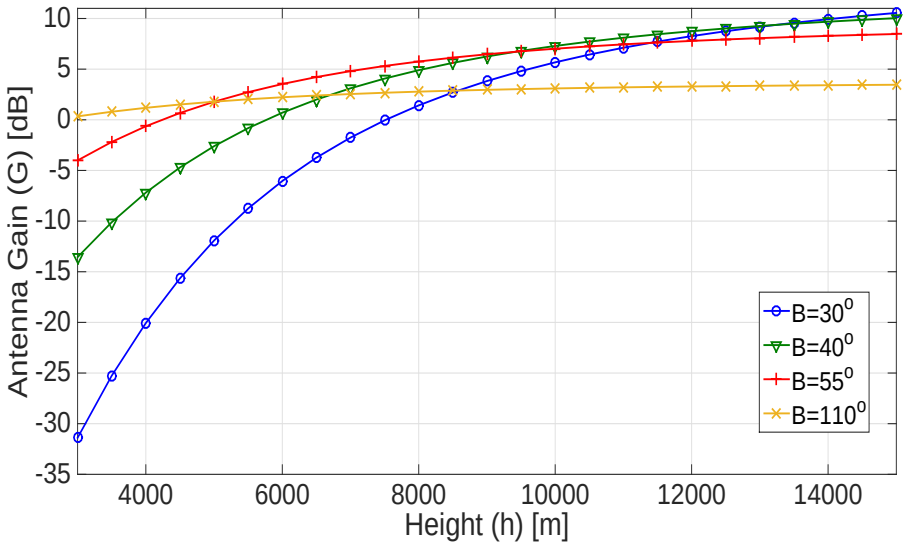

Fig. 4.6: Antenna gain at $r = 5000$m with varying heights for different beamwidths.

value of coverage radius in relation to antenna gain, for instance, maximum coverage radius of 5000m at a beamwidth of 55^o for $h = 7000$m in Fig. 4.5 can be attributed to the occurence of largest antenna gain at a beamwidth of 55^o at a height of 7000m in Fig. 4.6. This trend remains hidden in UAV coverage models presented in prior studies [19]-[42].

Fig. 4.7 shows the antenna gain plotted for $h = 3500$m as the coverage radius changes.

This figure, along with previous discussion on the interplay between factors affecting coverage radius simultaneously can be used to explain the radius vs. beamwidth trend of the three dimensional Fig. 4.3(a) earlier, which is also plotted for $h = 3500$m. The continuous decrease of coverage radius with increase in beamwidth for $r < 800$m in Fig. 4.3(a) can be attributed to the continuous decrease of antenna gain with radius in Fig. 4.7 for $r < 800$m. As we approach closer to 1000m, the trend in antenna gain pattern starts to reverse for different beamwidths, and we observe several intersecting points from $1000 < r < 2500$ in Fig. 4.7 and hence mean RSS in Fig. 4.3(b) attains a parabolic shape with increasing beamwidth in this range. At very large r, gain trend reverses completely and now it increases with increasing beamwidths, which is again inline with RSS trend in Fig. 4.3(c). Note also that at very large coverage radius, for example, at $r = 4000$m in Fig. 4.3(c), RSS decreases very sharply from 50^o to 30^o as compared to decrease in RSS from 120^o to 80^o. This is because at 4000m in Fig. 4.7, difference in gain between 50^o and 30^o is quite high (16dB) as compared to difference in gain between 120^o and 80^o (1dB).

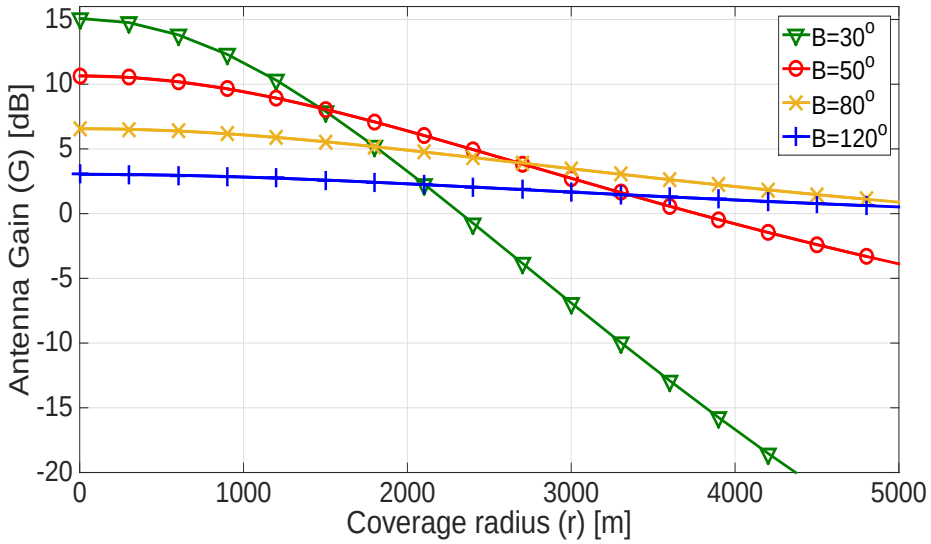

Fig. 4.7: Antenna gain at $h = 3500$m with varying radius for different beamwidths.

As shown by Fig. 4.3 and Fig. 4.5 and explained with the aid of Fig. 4.6 and Fig. 4.7, the UAV coverage model for the first time shows theexistence of optimal beamwidth for

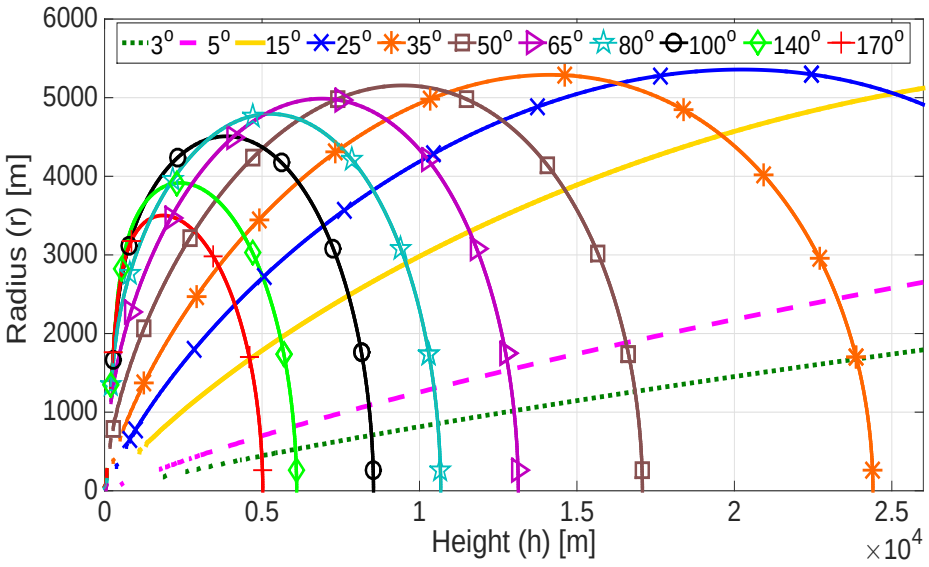

Fig. 4.8: Coverage radius against height for different beamwidths.

given height for maximum coverage radiusand vice versa. The model also provides an easy method to determine the optimal beamwidth/height for desired coverage radius in form of (4.1).

4.2 Coverage Radius vs Height

Fig. 4.8 depicts the relation of coverage radius with height for different beamwidths. Initially, as the height of the UAV increases for small beamwidths, coverage radius also increases continuously. However, as beamwidth increases further, coverage radius reaches a maximum point and then starts to decrease. These trends are again revealed due to consideration of all important aspects of the system model in this study. Previous studies that overlook one or more of these aspects suggest that UAV coverage radius increases monotonically as UAV altitude increases [42].

4.3 Height vs Beamwidth

Fig. 4.9 shows the relationship of height and beamwidth. Suppose a UAV is deployed to cover a fixed radius, r_f with a certain ϵ. The height vs beamwidth relationship in Fig.

4.9 answers the following question: If the height of UAV is changed after its deployment, how can the beamwidth be adjusted to restore UAV coverage radius back to r_f? It is applicable when height is subject to changes due to factors beyond system designer control such as weather etc, and same coverage pattern has to be maintained.

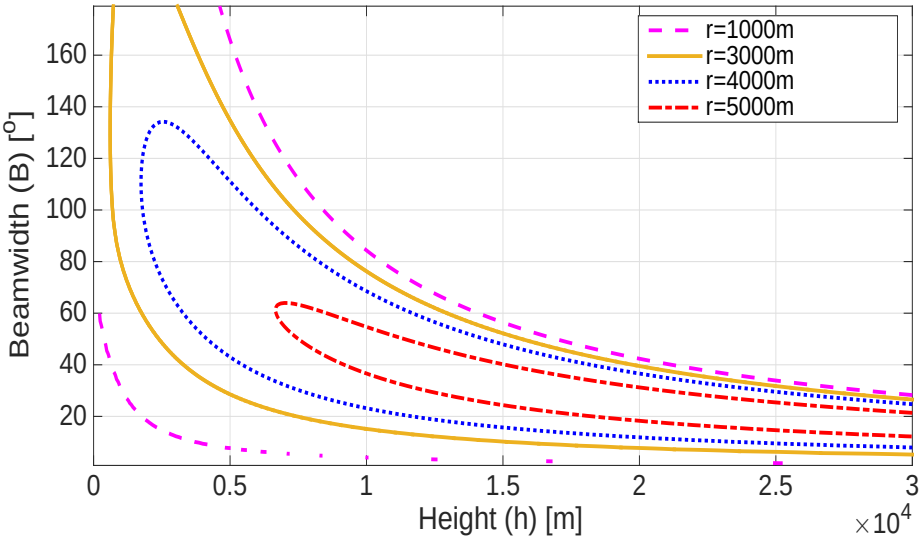

Fig. 4.9: Beamwidth against height for different radii.

Fig. 4.9 also highlights the importance of optimizing both beamwidth and height in tandem with each other rather than independently as opposed to prior works [19] and [42]. For example, if a UAV is deployed to cover $r_f = 4000$m with $\epsilon = 0.8$ at a height of 10000m and if its height is changed to 5000m, the UAV will need to adjust its beamwidth from 70^o to either 42^o or 110^o in order to continue providing the same coverage. On the other hand, if a UAV is deployed to cover a radius of 5000m with coverage probability of 0.8, it can not achieve the desired radius with the desired coverage threshold back if its height is changed to 2000m. An alternate representation of this can also observed from Fig. 4.5. If we draw a line at $r = 5000$m in Fig. 4.5, it will always be above the curve for $h = 2000$m.

CHAPTER 5

Analysis with Varying Frequency and Environment

Fig. 5.1 quantifies the variation of coverage radius with beamwidth for different environments at $h = 3000$m, $\epsilon = 0.8$ and $PL_{max} = 115$dB. Not only is the maximum coverage radius largest for suburban environment, followed by urban, dense urban and high rise urban environments, but also the beamwidth at which radius vs beamwidth trend reverses attains a lower value as environment becomes denser, i.e., for suburban environment, radius starts to decrease with increase in beamwidth at 80^o, whereas for high rise urban environment, this point reduces to 20^o.

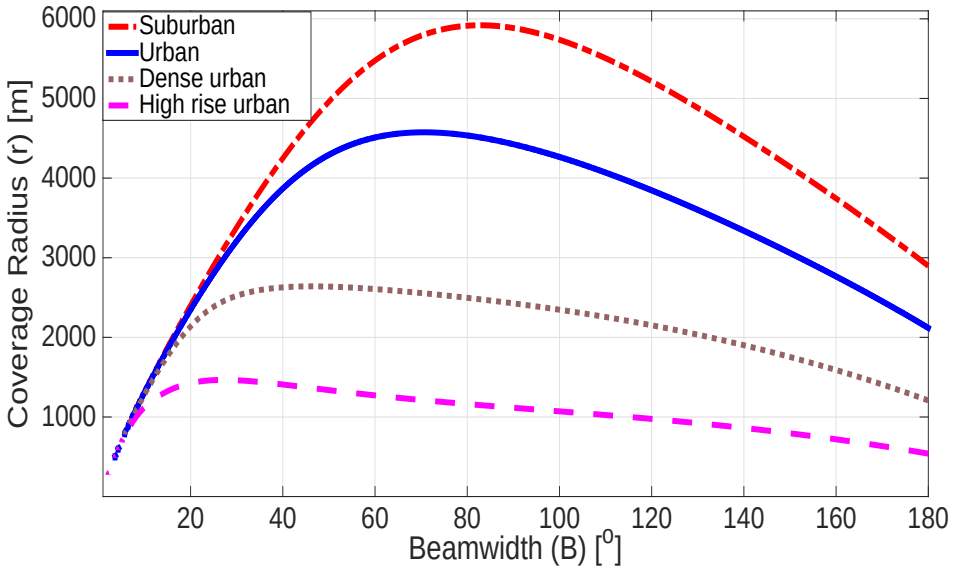

Fig. 5.1: Coverage radius with varying beamwidth for different environments at $h = 3000m$.

Next, the dimension of frequency is also added in the analysis. Fig. 5.2 quantifies the tradeoff of coverage radius with beamwidth in changing environments and at different frequencies for two extreme environments. The figure is plotted for $h = 3000$m, $PL_{max} = 120$dB for two extreme environments, suburban and high rise urban. Several observations can be made from the figure. Firstly, the achievable coverage radius

is greater in a suburban environment as compared to a high rise urban environment, mainly due to increased path loss in high rise urban environment. In addition to coverage radius decreasing sharply in dense urban environment, the beamwidth at which decrease in coverage radius starts also decreases in high rise urban environment. It can be observed from Fig. 5.2 that in high rise urban environments, decrease in radius starts from a beamwidth as low as 30^o at 2.0GHz, whereas for the same frequency, this decrease does not start until 110^o in case of the suburban environment.

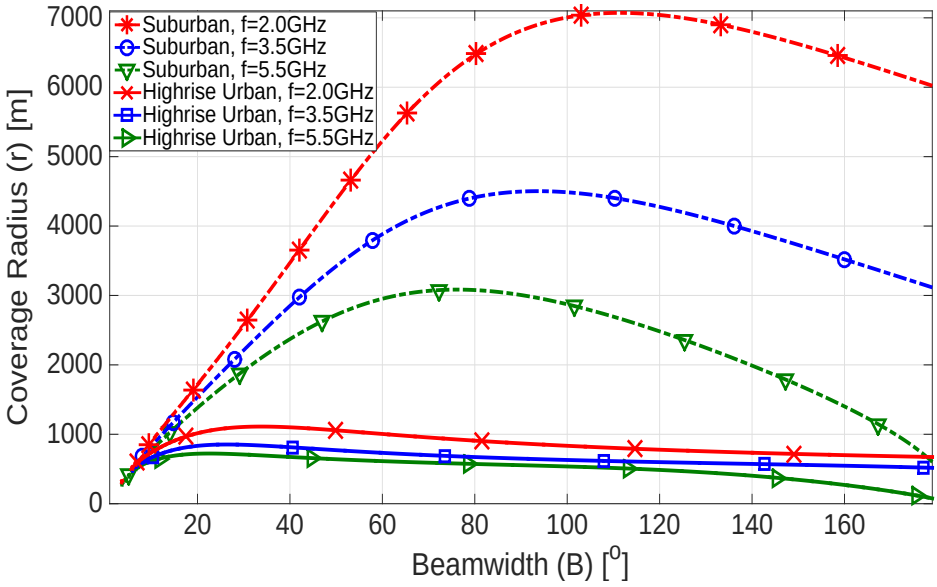

Fig. 5.2: Coverage radius against beamwidth for varying frequency and environment at $h = 3000$m.

Secondly, with increase in frequency, coverage radius decreases. Frequency plays an stronger role especially in suburban environment, since a higher frequency not only leads to a sharp decrease in coverage radius, but also reverses the trend of coverage radius vs. beamwidth at much lower beamwidths. As can be seen from Fig. 5.2, at 2.0 GHz in suburban environment, radius increases till 110^o beamwidth, but at 5.5 GHz radius starts to decrease with increasing beamwidth from 70^o onwards in the same suburban environment. This is not just because of free space path loss which increases with increasing frequency, but also because of the shadowing model, the mean of which is shown to increase at higher frequencies [50]. Another interesting insight can be

drawn from the figure: as we move towards denser environments, the difference between coverage radius of a UAV at different frequencies decreases. In other words, the impact of frequency reduces as environment becomes denser. These observations could play a valuable role for designing UAV based cellular systems at higher frequencies as exploiting higher frequencies by utilizing the unused part of frequency spectrum is a key research area nowadays.

CHAPTER 6

Impact of Altitude, Beamwidth and Radius on RSS distribution

Before studying the tradeoffs between key UAV deployment parameters on RSS as described by (3.13)-(3.16), validation of the proposed model is presented. Fig. 6.1 and Fig. 6.2 show PDF of RSL at two arbitrary points, located at $r = 3000$m for UAVs deployed at height of $h = 2000$m and beamwidths of $B = 5^o$ and 50^o respectively. Analytical expression derived in (3.15) is plotted and compared with simulation results. PDF obtained from the derived analytical expression and simulations are in excellent agreement. In Fig. 6.1, the beamwidth is very low, 5^o and hence users located at $r = 3000$m receive extremely low RSL as shown by the values on x-axis of the histogram. In contrast, when beamwidth is increased to 50^o, the same users start to receive a much better coverage i.e., between -85 to -65 dBm.

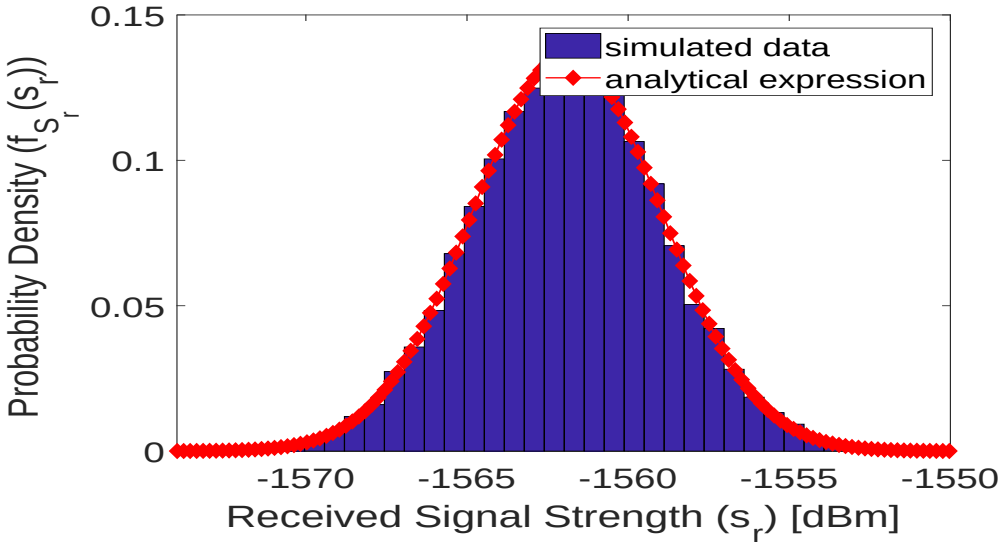

Fig. 6.1: PDF of RSS at $r = 3000$m, $B = 5^o$ and $h = 2000$m.

The analysis is extended from RSS at any arbitrary point in a given area to RSS inside

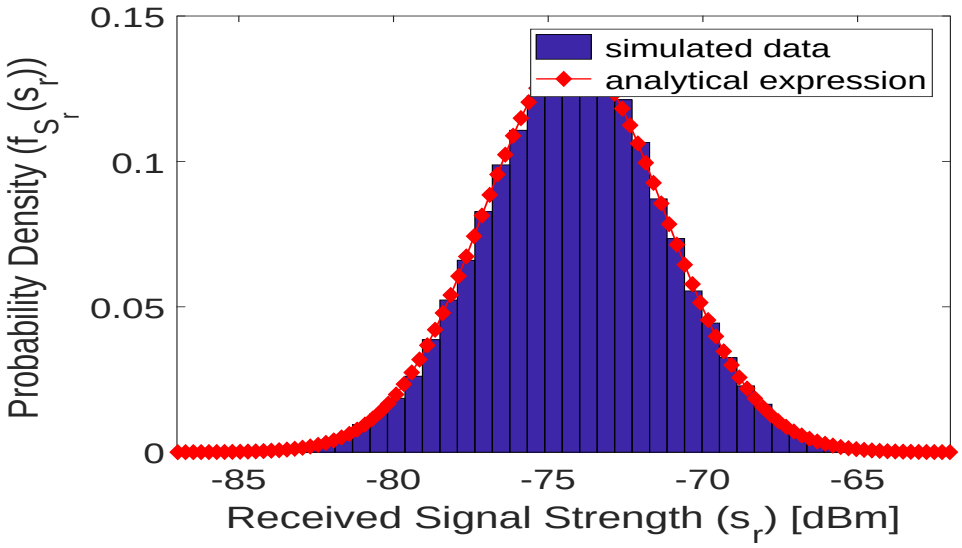

Fig. 6.2: PDF of RSS at $r = 3000$m, $B = 50^o$ and $h = 2000$m.

a geographical area. Fig. 6.3-6.4 show the footprint of RSS on ground in an area of $12000m$ x $12000m$. These figures are plotted for three different beamwidths: 5^o (low) 50^o (medium) and 120^o (high) and four different heights: 500m, 1500m, 3500m and 5500m. Key observation to be made here is that the range of RSS becomes narrower in a given area with either increasing beamwidth or increasing height. Further, the greatest value of RSS at the center of the cell is at lowest beamwidth due to highest antenna gain. However, a very small area out of the entire area gets good coverage because of low beamwidth. In fact, RSS decays sharply to negligible values as radius increases. As the beamwidth increases, RSS decreases at the cell center; however, a larger fraction of the total area is receiving good coverage in terms of higher values of received signal strength. Nonetheless, this might also cause higher interference with neighboring UAVs. Although this is out of scope of this study, it should be analyzed in future research.

To better illustrate the quantitative behaviour of RSS inside a cell, normalized histograms of RSS from the simulation results is shown in Fig. 6.6-6.7. Analytical PDF obtained through integration of expression derived in (3.15) through (3.16) is also plotted. The PDF derived from the analytical expression matches the simulation results. From Fig. 6.6-6.7, we can not only see the effect of beamwidth and height on the range

of RSS inside a cell, but also observe the shape of distribution of RSL. It is noted that it approaches Gaussian distribution with increasing height or increasing beamwidth.

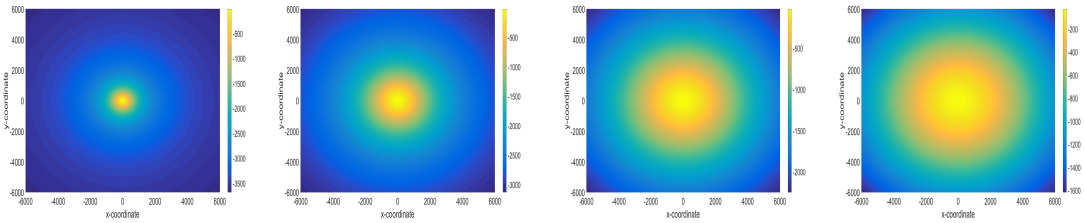

(a) $h = 500$m (b) $h = 1500$m (c) $h = 3500$m (d) $h = 5500$m

Fig. 6.3: RSS footprint with changing altitude of UAV for $B = 5^o$

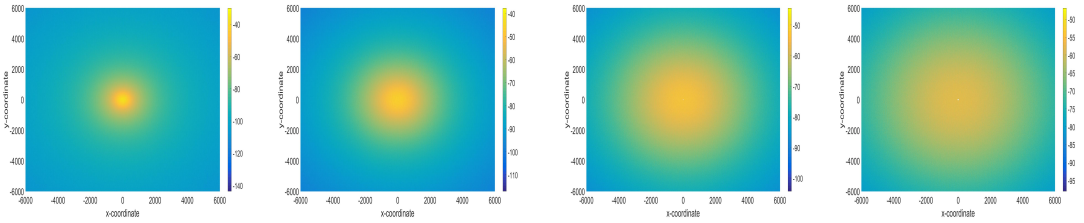

(a) $h = 500$m (b) $h = 1500$m (c) $h = 3500$m (d) $h = 5500$m

Fig. 6.4: RSS footprint with changing altitude of UAV for $B = 50^o$

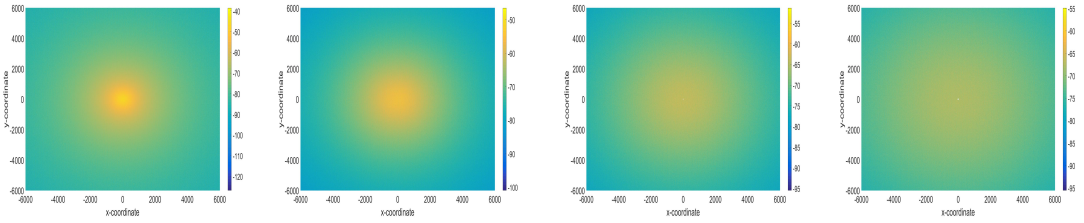

(a) $h = 500$m (b) $h = 1500$m (c) $h = 3500$m (d) $h = 5500$m

Fig. 6.5: RSS footprint with changing altitude of UAV for $B = 120^o$

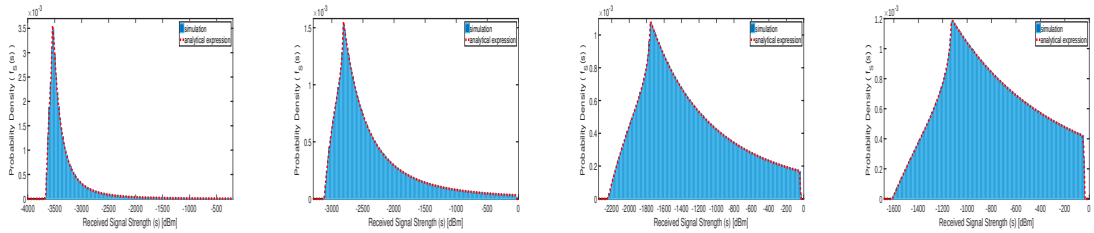

(a) $h = 500$m (b) $h = 1500$m (c) $h = 3500$m (d) $h = 5500$m

Fig. 6.6: PDF of RSS on ground with changing altitude of UAV for $B = 5^o$

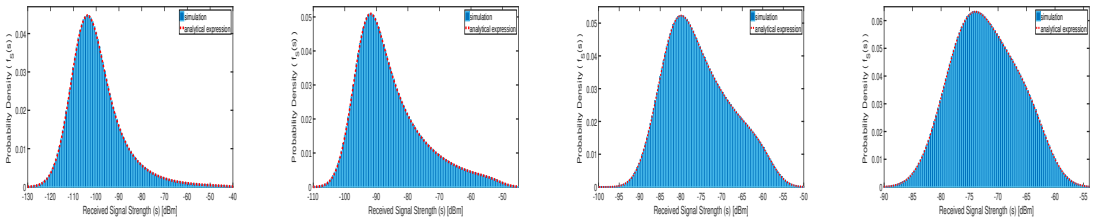

(a) $h = 500$m (b) $h = 1500$m (c) $h = 3500$m (d) $h = 5500$m

Fig. 6.7: PDF of RSS on ground with changing altitude of UAV for $B = 50^o$

CHAPTER 7

Comparison of Altitude and Beamwidth to Control Coverage

Based on they analysis of beamwidth and height on coverage radius so far, it can be concluded that both beamwidth and height can be used for the same purpose of controlling coverage. However, beamwidth is a more practical optimization parameter to control coverage because of physical and technical constraints on altitude imposed by earth's atmospheric layers and aviation regulations. Now, both of these parameters are compared by analyzing the relative effect of each of these parameters on coverage area. More specifically, the comparison is based on the sensitivity of coverage radius to each of these parameters. For this, we choose the metric of rate of change of coverage radius with beamwidth and height, i.e., how much the coverage radius changes with a unit change in beamwidth or height.

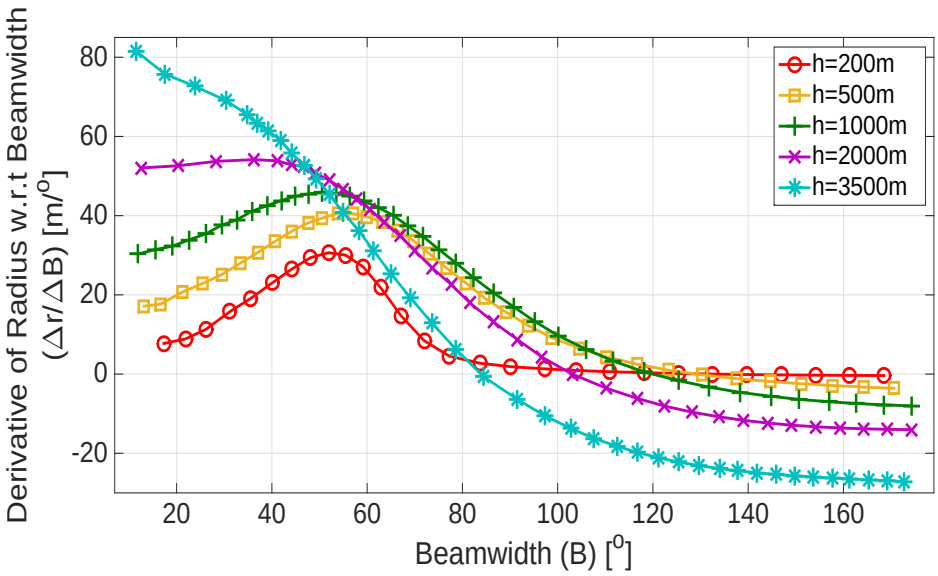

Fig. 7.1: Gradient of coverage radius with respect to beamwidth.

Fig. 7.1 shows the gradient of radius with respect to beamwidth for heights of upto 3500m. This plot is obtained by differentiating (3.7) with respect to beamwidth or

taking gradient of the curves in Fig. 4.5 with respect to beamwidth. We observe that maximum value of positive $\Delta r/\Delta B$ occurs at a altitudes 3500m. This suggests that radius is more sensitive to beamwidth at a height of 3500m as compared to heights ranging from 200m-2000m.

However, changing height can lead to decrease in coverage radius as well as previously shown by Fig. 4.5. This occurs mainly at lower beamwidths. Hence, beamwidths in the range of 1^o to 90^o are separately analyzed in in Fig. 7.2. Over here, it is observed that the decrease in coverage radius is most sensitive to very high heights of 25000m.

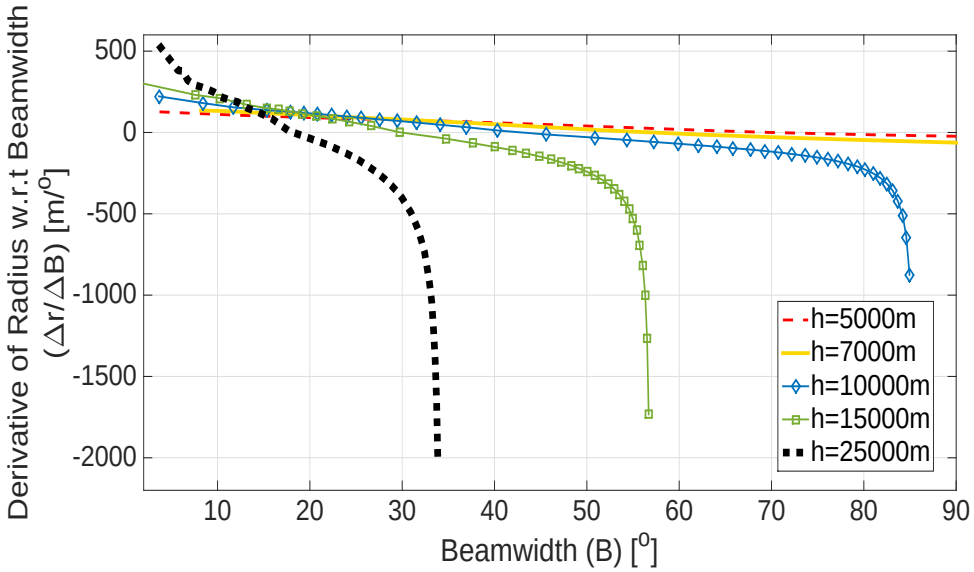

Fig. 7.2: Gradient of coverage radius with respect to beamwidth for different heights in low beamwidth regime.

Next, the rate of change of radius with height ($\Delta r/\Delta h$) is analyzed in Fig. 7.3 obtained by differentiating (3.7) w.r.t to height or taking the gradient of the curves in Fig. 4.8. Unlike Fig.7.1, the values of derivatives here follow a similar pattern with changing beamwidths except for beamwidths $< 25^o$ where $\Delta r/\Delta h$ is constant. For beamwidths $> 25^o$, $\Delta r/\Delta h$ first decreases to 0 and then increases in the negative direction. By comparing values of the derivative in Fig. 7.3 with Fig. 7.1-7.2 (both comparisons range from samples of heights from between 0 to 25000m and beamwidths from 1^o to 180^o), we note that $\max(\Delta r/\Delta B) >> \max(\Delta r/\Delta h)$. Numerically, the maximum

value of max($\Delta r/\Delta B$), -2000 is almost 75 times greater than the maximum value of max($\Delta r/\Delta h$), -27.

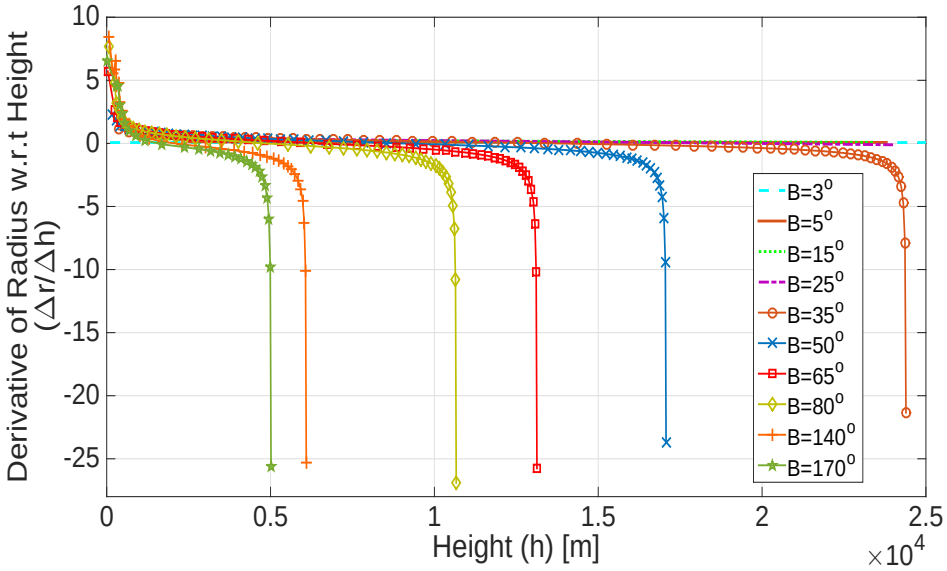

Fig. 7.3: Gradient of coverage radius with respect to height.

This indicates that radius is more sensitive to low beamwidths as compared to height, i.e., low beamwidths lead to greatest change (decrease) in coverage radius as compared to the entire range of heights. This inference is in agreement with previous results as well, such as Fig. 4.5, which shows a sharp decrease in coverage radius at low beamwidths and Fig. 6.1 and Fig. 6.3(a)-6.3(d) which show that RSL decays rapidly with increasing r at low beamwidths.

CHAPTER 8

Multiple UAVs

In this chapter, the analysis is extended to cover a target geographical area with a certain coverage threshold using multiple UAVs. Specifically, following aspects are studied: finding the minimum number of UAVs required to cover a given area with certain coverage threshold requirements, the beamwidth needed to cover maximum possible area for a given number of UAVs and effect of UAV altitude as the number of UAVs vary. The findings are then compared with prior literature and reveal several important insights that previous over-simplified models do not reveal.

To address such problems, a UAV placement model is needed. Previous literature [42], utilizes circle packing theory to place UAVs in a certain geographical area. In the circle packing problem, N identical circles (cells) should be arranged inside a larger circle (target area) of radius R_t such that the packing density is maximized and none of the circles overlap [53]. The radius of each of the N circles that solves this problem is denoted by r_{max} and one UAV provides coverage to one small cell (circle). However, this solution has two caveats. Firstly, significant gaps between circles or cells are inevitable when two or more circles are used to cover a given area. This is due to the inherent nature of utilizing circle packing theory, since in order to strictly cover the target area completely, $N \to \infty$ and $r_{max} \to 0$. Alternatively, an infinite number of circles with zero radii are required to completely cover a circular area. Secondly, the number of circles (UAVs) increase rapidly with coverage probability. We overcome both of these problems by introducing a UAV placement model based on hexagonal cells. This model not only resolves aforementioned problems but also leads to a better coverage. In the hexagonal packing problem, N identical regular hexagons are arranged inside a larger hexagon such that the packing density is maximized, none of the hexagons overlap and

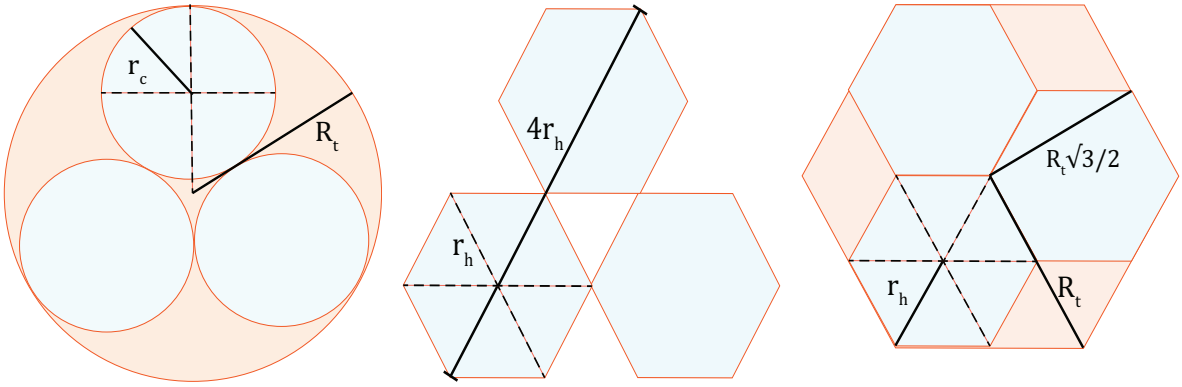

(a) Circle packing (b) Max. distance between hexagons (c) Hexagon packing

Fig. 8.1: Circle packing and hexagonal packing for $N = 3$.

no gap is left between adjacent hexagons. As an example, consider the case for $N = 3$ in Fig. 8.1. If we consider a hexagonal area with the longest distance from center to the edge denoted by R_t and the distance from center to the vertex of a hexagon by r_h, then the maximum distance between any two farthest hexagons will be $4r_h$ as shown in Fig. 8.1(b). Our goal is to minimize this distance in order to maximize the packing density. Clearly, this can be possible only if all hexagons are arranged adjacent to each other without leaving any gap in between. This leads to the arrangement shown in Fig. 8.1(c). Here, the maximum distance between farthest hexagons is $4r_h\sqrt{3}/2 < 4r_h$. This leads to $r_h = 0.5R_t = r_{max}$. The maximum total coverage (in percentage) for $N = 3$ can then be calculated as follows:

$$C_h = \frac{\text{area covered by 3 UAVs}}{\text{total area to be covered}} = \frac{3\left(\frac{3}{2}\sqrt{3}\left(\frac{1}{2}R_t\right)^2\right)}{\frac{3}{2}\sqrt{3}R_t^2} = 75\% \tag{8.1}$$

Note that r_h is also the longest distance from center to the edge of the hexagon. Denoting the longest distance by r_h is important because of the way the problem is formulated in Section III, i.e, we find maximum possible r for a given threshold. Therefore, if users on the cell edge located at r_h satisfy the given threshold requirement, the users located at $r < r_h$ are bound to satisfy that threshold as well. Fig. 8.1(a) shows the geometry of circle packing theory for comparison.

Similar analysis is done for $N = 1$ to 10 and presented in Table 8.1. In the table, C_c and C_h represents the maximum percentage of actual area covered out of total target area using circular and hexagonal packing respectively while r^c_{max} and r^h_{max} represent the maximum possible radius of each cell using the two approaches. Columns 2 and 4 are from [42] and used as a benchmark for comparison with the proposed packing strategy. From the proposed approach, we can observe that the maximum possible coverage is at least 69.2% (∼70 %) for any number of UAVs using hexagonal cells, whereas it drops to as low as 50% using circle packing theory. This has a direct impact on the coverage threshold requirement of the system. For example, it is highlighted in [42] that a 0.7 coverage performance is impossible to achieve with $1 < N < 7$ using circle packing approach. Our proposed hexagonal packing strategy, on the other hand, ensures that this coverage performance demand can be met with any number of UAVs. We illustrate this by selecting different geographical areas, denoted by parameter, R_t and calculating the minimum number of UAVs required to cover it for a coverage threshold $\geq 70\%$, with a tolerance of $\pm 1\%$.

Table 8.1: Comparison between circular and hexagonal packing in terms of coverage radius of each UAV and maximum total coverage.

N	r^c_{max}	r^h_{max}	C_c	C_h
1	R_t	R_t	1	1
2	$0.500R_t$	$0.447R_t$	50.0	75.0
3	$0.464R_t$	$0.500R_t$	64.6	75.0
4	$0.413R_t$	$0.400R_t$	68.6	75.0
5	$0.370R_t$	$0.333R_t$	68.5	75.0
6	$0.333R_t$	$0.286R_t$	66.6	75.0
7	$0.333R_t$	$0.333R_t$	77.8	77.8
8	$0.302R_t$	$0.286R_t$	73.3	72.7
9	$0.275R_t$	$0.250R_t$	68.9	69.2
10	$0.261R_t$	$0.286R_t$	68.7	75.0

In order to determine the minimum number of UAVs, first, the maximum possible coverage radius of each UAV (r_{max}) is determined for a given PL_{max} and ϵ over a range of height and beamwidth. For a $\text{PL}_{\text{max}} = 115\text{dB}$ and $\epsilon = 0.8$ over $0 < h \leq 5000$ and $1 < B < 180$, r_{max} turns out to be 4800m (Fig. 4.5). Next, for each R_t, possible values of UAVs and corresponding r^h_{max} are calculated using Table 8.1 based on the given coverage threshold. Only those rows of r^h_{max} and r^c_{max} are used that satisfy 70 $\pm$1% coverage threshold. Finally, based on r_{max} (i.e., calculated r^h_{max} should be less than r_{max}), we determine how many UAVs are needed for each R_t again using Table 8.1. Fig. 8.2 compares the resulting minimum number of UAVs obtained with hexagonal packing and circle packing from [42]. For $C = 70\%$, from circle packing approach, we can cover a desired area upto 14 km with only 1, 7 or 8 UAVs. On the other hand, with the proposed hexagonal packing approach, we can cover an area with a much smaller number of UAVs, i.e., 1, 2, 4 or 5 UAVs.

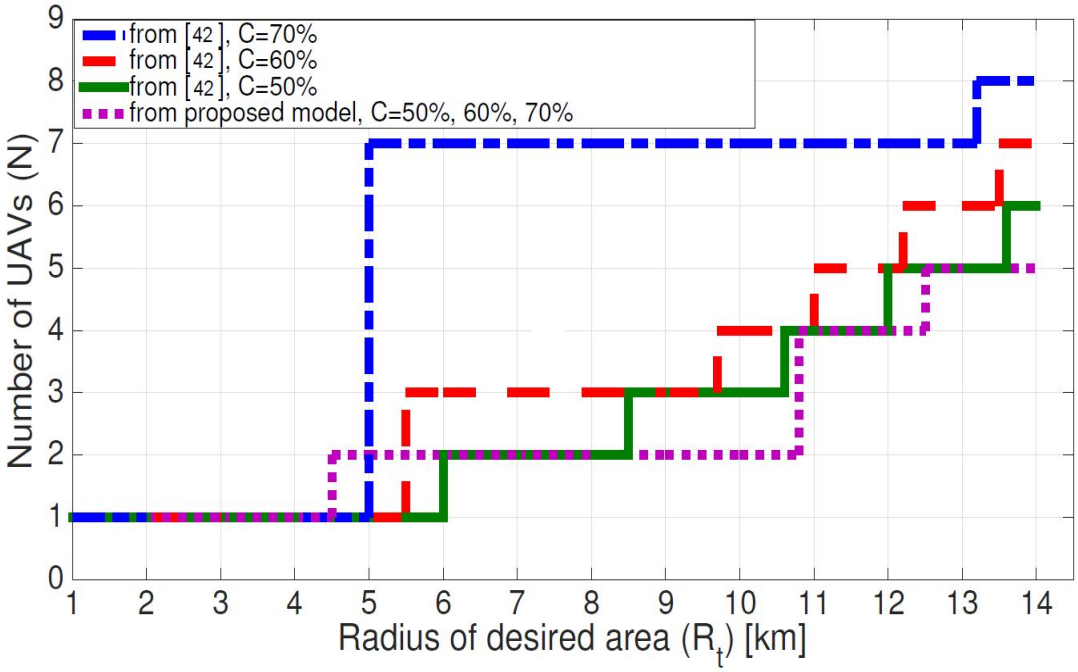

Fig. 8.2: Minimum number of UAVs verses radius of desired area for different minimum coverage thresholds.

Another advantage that hexagonal packing offers is the relative scalability of number of UAVs as the coverage threshold changes, which in case of circle packing increases

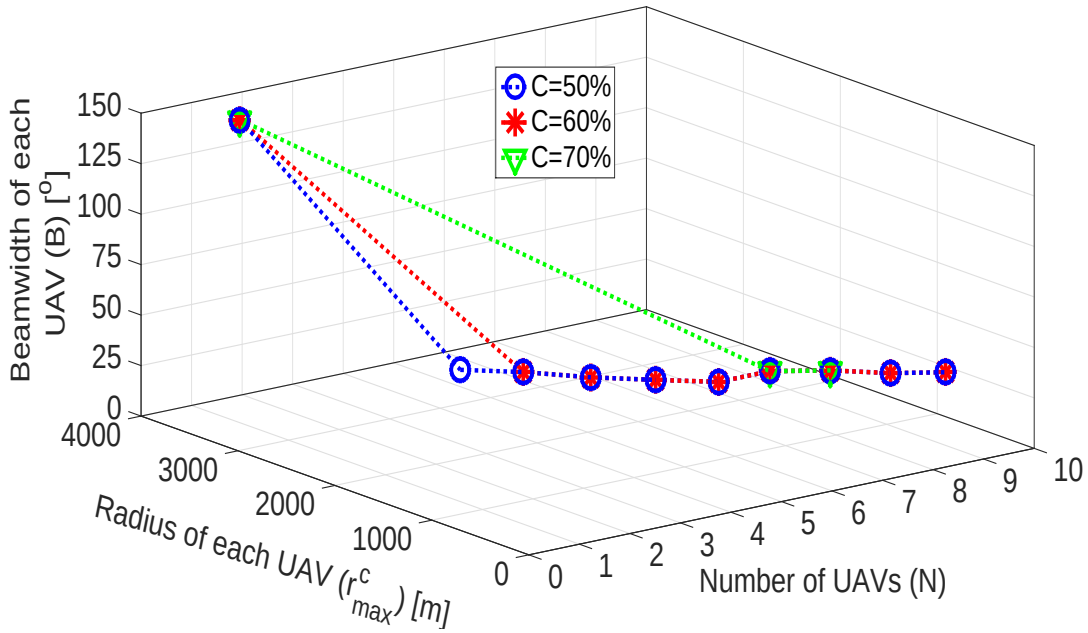

Fig. 8.3: Optimal beamwidth for multiple UAVs and corresponding radius of each UAV.

rapidly as coverage threshold goes from 50% to 80% as seen in Fig. 8.2.

In order to draw further insights from the model capturing effect of 3D directional antenna, we investigate the relationship between number of UAVs and beamwidth of each UAV. First, we find the maximum possible r for a given geographical area with radius R_t using Table 8.1 as the number of UAVs vary and then the corresponding beamwidth using Fig. 4.5 from the proposed model. Fig. 8.3 illustrates the results for a UAV deployed at a height of 1000m in a suburban environment. The target geographical area to be covered is $R_t = 3500$m. We can observe an overall decreasing trend between beamwidth and number of UAVs for different coverage requirements. This quantifies the intuitive observation that we can either cover the same area with a single UAV having a wide beamwidth or with multiple UAVs having narrow beamwidths. For example, for a coverage threshold of 60%, we can cover a target area of radius 3500m either with 10 UAVs, each having a beamwidth of 22^o or with a single UAV having a beamwidth of 150^o. Our model allows use of more design options for a wireless system designer with regards to conservation of infrastructure.

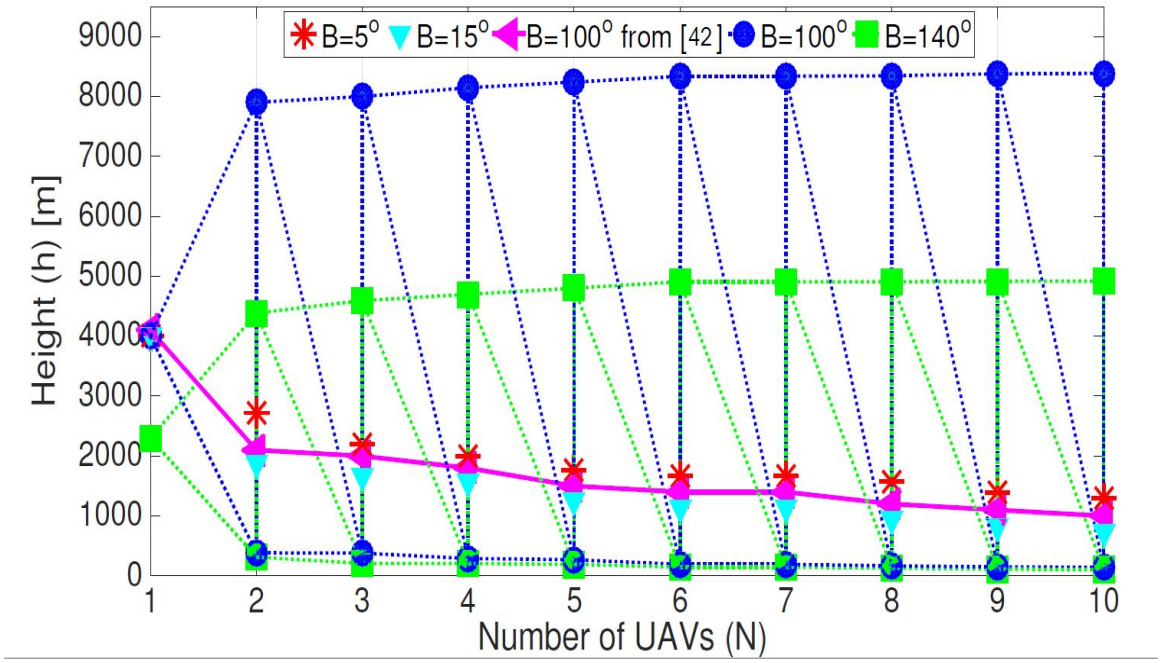

Fig. 8.4: Altitude with varying no. of UAVs for different beamwidths.

Finally, in order to observe the trend of UAV altitude as the number of UAVs vary, the optimal UAV altitude that will yield maximum possible coverage is plotted in Fig. 8.4 for different number of UAVs. The system model using binary antenna gain pattern proposed in [42] does not reflect the role of beamwidth in UAV altitude with increasing number of UAVs. Hence, UAV altitude decreases monotonically as number of UAVs increases. Fig. 8.4 shows this is not the case when a practical antenna gain pattern, as proposed in this study, is used. In the plot, one UAV covers maximum possible area for a certain beamwidth that can be found from Fig. 4.8. For beamwidths upto 15^o, UAV altitude with number of UAVs follow the same trend as in [42]. However, the trend changes for higher beamwidths. As can be seen from Fig. 4.8, for any coverage radius less than the maximum radius and $B > 15^o$, there are two possible options for UAV altitude. Note that after $N > 2$, height of UAV increases or decreases at a much slower rate in Fig. 8.4 . This is because the rate of change of radius with height for $B > 15^o$ in Fig. 4.8 is extremely high below $R/2$. This trend is explicitly compared with the model in [42] for a beamwidth of 100^o. We conclude that it is not necessary for UAV altitude to decrease monotonically as the number of UAV increases; in fact,

it can also either increase monotonically or behave as a combination of increasing and decreasing altitude as the number of UAVs increase. Our analysis can also be exploited for interference management in the presence of other aerial platforms since it provides multiple altitude options for UAV deployment, thus leading to more flexible design options which is imperative to the design of next generation cellular systems. Such investigations of interference using proposed model can be focus of a future study.

CHAPTER 9

Conclusion and Future Work

This thesis provides a holistic analysis of the interplay between key UAV deployment parameters: coverage radius, height and beamwidth while considering design space dimensions that remain unexplored in existing studies. It further provides a mathematical model to estimate RSS at any distance from boresight of antenna as a function of antenna beamwidth and altitude.

The analysis and results provides several new insights that prior models with no or simplified antenna, path loss, or shadowing models fail to reveal, such as: 1) UAV altitude or antenna beamwidth does not have to necessarily increase continuously for higher coverage radius; 2) contrary to findings reported in some prior studies, UAV coverage radius does not necessarily increase as altitude increases and 3) the minimum number of UAVs required to cover a given area does not necessarily decrease monotonically as UAV altitude increases. These results allow us to determine optimal parameters for realistic deployment.

Furthermore, based on the analysis of effect of beamwidth and altitude on coverage radius, it is found that antenna beamwidth and altitude should be optimized simultaneously rather than independently as is the case assumed in previous works. It is also concluded that optimizing beamwidth instead of height to control coverage may be a more practical optimization parameter and that coverage is most sensitive to beamwidths of less than 40^o. A hexagonal packing is proposed in case of multiple UAVs, which would although introduce more interference on boundary areas as compared to circle packing; however, it does not leave any coverage holes, can cover a higher proportion of the given area and is scalable in terms of number of UAVs with increasing area.

Future work would include optimization of deployment parameters in multiple UAVs scenario while considering interference between UAVs and tilt angle optimization. Tools from machine learning and stochastic optimization will be used to address such problems. Self healing of airborne networks could also be addressed. Another direction is investigating the various aspects of air-to-ground systems by using massive MIMO, either as UAVs acting as aerial base stations with large number of antennas (3D antenna arrays) or ground base stations equipped with large number of antennas providing connectivity to UAVs with single receive antennas. The ideas proposed in this thesis can also be extended to applications of airplanes with additional issues such as doppler shift.

List of Key Symbols

h	height of UAV
r	coverage radius
d	UAV to MS distance
c	speed of light
f	frequency
N	number of UAVs
P_l	probability of LoS link
P_n	probability of NLoS link
X_l	RV to account for LoS location variability
X_n	RV to account for NLoS location variability
X_s	RV shadowing
X'_n	$X'_n = X_n + X_s$
σ_l	standard deviation of X_l
σ_n	standard deviation of X_n
μ'_n	mean of X'_n
σ'_n	standard deviation of X'_n
μ_{sh}	mean of X_s
σ_{sh}	standard deviation of X_s
ϕ_{tilt}	tilt angle of antenna
ϕ_{MS}	vertical angle from reference axis for tilt to MS
θ_a	azimuth angle of antenna w.r.t horizontal reference axis
θ_{MS}	angular distance of MS
B_{NS}	beamwidth in North-South direction
B_{EW}	beamwidth in East-West direction

B	beamwidth for circular beam pattern
λ_{NS}	weighting factor for beam pattern in North-South direction
λ_{EW}	weighting factor for beam pattern in East-West direction
G	antenna gain
G_{max}	maximum antenna gain at bore sight
$A_{\max}$	maximum antenna attenuation at sides and back of bore sight
PL_{max}	maximum pathloss
R_t	radius of desired geographical area
ϵ	minimum coverage probability
γ	received signal threshold
S_n	NLoS component of received signal at any r: $S_n = P_n R_n$
S_l	LoS component of received signal at any r: $S_l = P_l R_l$
σ_{s_l}	standard deviation of S_l
σ_{s_n}	standard deviation of S_n
R_l	LoS received signal
R_n	NLoS received signal
S_r	received signal at any r: $S_r = S_l + S_n$
σ_s	standard deviation of S_r
S	received signal inside a geographical region
μ_s	mean of S_r
P_{cov}	coverage probability
T	transmit signal
$f_S(s)$	PDF of S
$f_{S_r}(s_r)$	PDF of S_r

Bibliography

[1] A. Imran and R. Tafazolli, "Performance & capacity of mobile broadband WiMAX (802.16 e) deployed via high altitude platform," in *IEEE European Wireless Conference*, 2009, pp. 319–323.

[2] A. Imran, M. Shateri, and R. Tafazolli, "On the comparison of performance, capacity and economics of terrestrial base station and high altitude platform based deployment of 4G," in *Proceedings of the 6th ACM Symposium on Performance Evaluation of Wireless Ad Hoc, Sensor, and Ubiquitous Networks*, 2009, pp. 58–62.

[3] Y. Zeng, R. Zhang, and T. J. Lim, "Wireless communications with unmanned aerial vehicles: opportunities and challenges," *IEEE Communications Magazine*, vol. 54, no. 5, pp. 36–42, 2016.

[4] T. Nakamura, S. Nagata, A. Benjebbour, Y. Kishiyama, T. Hai, S. Xiaodong, Y. Ning, and L. Nan, "Trends in small cell enhancements in LTE advanced," *IEEE Communications Magazine*, vol. 51, no. 2, pp. 98–105, 2013.

[5] S. Rangan, T. S. Rappaport, and E. Erkip, "Millimeter-wave cellular wireless networks: Potentials and challenges," *Proceedings of the IEEE*, vol. 102, no. 3, pp. 366–385, 2014.

[6] G. Maral and M. Bousquet, *Satellite Communications Systems: Systems, Techniques and Technology*. John Wiley & Sons, 2011.

[7] K. Gomez, T. Rasheed, L. Reynaud, and S. Kandeepan, "On the performance of aerial LTE base-stations for public safety and emergency recovery," in *IEEE GLOBECOM Workshops (GC Wkshps)*, 2013, pp. 1391–1396.

[8] A. Al-Hourani and S. Kandeepan, "Cognitive relay nodes for airborne LTE emergency networks," in *7th International Conference on Signal Processing and Communication Systems (ICSPCS)*, 2013, pp. 1–9.

[9] Z. Shao, Y. Liu, Y. Wu, and L. Shen, "A rapid and reliable disaster emergency mobile communication system via aerial ad hoc BS networks," in *7th International Conference on Wireless Communications, Networking and Mobile Computing*, 2011, pp. 1–4.

[10] W. H. Robinson and A. P. Lauf, "Resilient and efficient MANET aerial communications for search and rescue applications," in *International Conference on Computing, Networking and Communications (ICNC)*, 2013, pp. 845–849.

[11] S. Karapantazis and F. Pavlidou, "Broadband communications via high-altitude platforms: A survey," *IEEE Communications Surveys Tutorials*, vol. 7, no. 1, pp. 2–31, First 2005.

[12] S. Rohde and C. Wietfeld, "Interference aware positioning of aerial relays for cell overload and outage compensation," in *IEEE Vehicular Technology Conference (VTC Fall)*, 2012, pp. 1–5.

[13] K. Daniel and C. Wietfeld, "Using public network infrastructures for UAV remote sensing in civilian security operations," DTIC Document, Report, 2011.

[14] H. S. Dhillon, H. Huang, and H. Viswanathan, "Wide-area wireless communication challenges for the Internet of Things," *IEEE Communications Magazine*, vol. 55, no. 2, pp. 168–174, 2017.

[15] S. Y. Lien, K. C. Chen, and Y. Lin, "Toward ubiquitous massive accesses in 3GPP machine-to-machine communications," *IEEE Communications Magazine*, vol. 49, no. 4, pp. 66–74, 2011.

[16] M. Mozaffari, W. Saad, M. Bennis, and M. Debbah, "Mobile unmanned aerial vehicles (UAVs) for energy-efficient internet of things communications," *arXiv preprint arXiv:1703.05401*, 2017.

[17] M. Mozaffari, W. Saad, M. Bennis, and Debbah, "Mobile internet of things: Can uavs provide an energy-efficient mobile architecture?" in *IEEE Global Communications Conference (GLOBECOM)*, 2016, pp. 1–6.

[18] N. H. Motlagh, T. Taleb, and O. Arouk, "Low-altitude unmanned aerial vehicles-based internet of things services: Comprehensive survey and future perspectives," *IEEE Internet of Things Journal*, vol. 3, no. 6, pp. 899–922, 2016.

[19] A. Al-Hourani, S. Kandeepan, and S. Lardner, "Optimal LAP altitude for maximum coverage," *IEEE Wireless Communications Letters*, vol. 3, no. 6, pp. 569–572, 2014.

[20] M. Mozaffari, W. Saad, M. Bennis, and M. Debbah, "Drone small cells in the clouds:

Design, deployment and performance analysis," in *IEEE Global Communications Conference (GLOBECOM)*, 2015, pp. 1–6.

[21] F. Qixing, J. McGeehan, E. K. Tameh, and A. R. Nix, "Path loss models for air-to-ground radio channels in urban environments," in *IEEE 63rd Vehicular Technology Conference*, vol. 6, 2006, pp. 2901–2905.

[22] M. Mozaffari, W. Saad, M. Bennis, and M. Debbah, "Unmanned aerial vehicle with underlaid device-to-device communications: Performance and tradeoffs," *IEEE Transactions on Wireless Communications*, vol. 15, no. 6, pp. 3949–3963, 2016.

[23] Y. Liu, D. Grace, and P. D. Mitchell, "Exploiting platform diversity for GoS improvement for users with different high altitude platform availability," *IEEE Transactions on Wireless Communications*, vol. 8, no. 1, pp. 196–203, Jan 2009.

[24] D. Eynard, P. Vasseur, C. Demonceaux, and V. Fremont, "UAV altitude estimation by mixed stereoscopic vision," in *2010 IEEE/RSJ International Conference on Intelligent Robots and Systems*, Oct 2010, pp. 646–651.

[25] J. Thornton, D. Grace, M. H. Capstick, and T. C. Tozer, "Optimizing an array of antennas for cellular coverage from a high altitude platform," *IEEE Transactions on Wireless Communications*, vol. 2, no. 3, pp. 484–492, May 2003.

[26] J. Thornton and D. Grace, "Effect of lateral displacement of a high-altitude platform on cellular interference and handover," *IEEE Transactions on Wireless Communications*, vol. 4, no. 4, pp. 1483–1490, July 2005.

[27] N. Goddemeier, K. Daniel, and C. Wietfeld, "Coverage evaluation of wireless networks for unmanned aerial systems," in *2010 IEEE GlLOBECOM Workshops*, Dec 2010, pp. 1760–1765.

[28] J. KoÅąmerl and A. Vilhar, "Base stations placement optimization in wireless networks for emergency communications," in *IEEE International Conference on Communications Workshops (ICC)*, 2014, pp. 200–205.

[29] Y. Zeng and R. Zhang, "Energy-efficient UAV communication with trajectory optimization," *IEEE Transactions on Wireless Communications*, vol. 16, no. 6, pp. 3747–3760, June 2017.

[30] M. Helmy, T. BaykaÅ§, and H. Arslan, "Optimization of aerial base station location in lap for disaster situations," in *2015 IEEE Conference on Standards for Communications and Networking (CSCN)*, Oct 2015, pp. 240–244.

[31] J. Lyu, Y. Zeng, R. Zhang, and T. J. Lim, "Placement optimization of UAV-mounted mobile base stations," *IEEE Communications Letters*, vol. 21, no. 3, pp. 604–607, March 2017.

[32] R. I. Bor-Yaliniz, A. El-Keyi, and H. Yanikomeroglu, "Efficient 3-D placement of an aerial base station in next generation cellular networks," in *IEEE International Conference on Communications (ICC)*, May 2016, pp. 1–5.

[33] A. Al-Hourani and S. Kandeepan, "Cognitive relay nodes for airborne LTE emergency networks," in *7th International Conference on Signal Processing and Communication Systems (ICSPCS)*, 2013, pp. 1–9.

[34] M. Alzenad, A. El-Keyi, F. Lagum, and H. Yanikomeroglu, "3-D placement of an unmanned aerial vehicle base station (UAV-BS) for energy-efficient maximal coverage," *IEEE Wireless Communications Letters*, vol. 6, no. 4, pp. 434–437, Aug 2017.

[35] H. Shakhatreh, A. Khreishah, J. Chakareski, H. B. Salameh, and I. Khalil, "On the continuous coverage problem for a swarm of UAVs," in *Sarnoff Symposium, 2016 IEEE 37th.* IEEE, 2016, pp. 130–135.

[36] H. A. Fayed and A. F. Atiya, "A mixed breadth-depth first strategy for the branch and bound tree of euclidean k-center problems," *Computational Optimization and Applications*, vol. 54, no. 3, pp. 675–703, 2013.

[37] A. Srinivas, G. Zussman, and E. Modiano, "Construction and maintenance of wireless mobile backbone networks," *IEEE/ACM Transactions on Networking (TON)*, vol. 17, no. 1, pp. 239–252, 2009.

[38] E. Yanmaz, "Connectivity versus area coverage in unmanned aerial vehicle networks," in *2012 IEEE International Conference on Communications (ICC)*, June 2012, pp. 719–723.

[39] E. Kuiper and S. Nadjm-Tehrani, "Mobility models for uav group reconnaissance applications," in *2006 International Conference on Wireless and Mobile Communications (ICWMC'06)*, July 2006, pp. 33–33.

[40] D. Orfanus, E. P. d. Freitas, and F. Eliassen, "Self-organization as a supporting paradigm for military UAV relay networks," *IEEE Communications Letters*, vol. 20, no. 4, pp. 804–807, 2016.

[41] F. Ono, H. Ochiai, and R. Miura, "A wireless relay network based on unmanned aircraft system with rate optimization," *IEEE Transactions on Wireless Communications*, vol. 15, no. 11, pp. 7699–7708, Nov 2016.

[42] M. Mozaffari, W. Saad, M. Bennis, and M. Debbah, "Efficient deployment of multiple unmanned aerial vehicles for optimal wireless coverage," *IEEE Communications Letters*, vol. 20, no. 8, pp. 1647–1650, 2016.

[43] "Unmanned systems antennas airborne platforms, UAVs, ground vehicles, robots," *UMS Antennas Issue 3, Cobham Antenna Systems, European Antennas Limited*, p. 3, 2010.

[44] A. Rocha, A. M. Correia, H. Adeli, R. L. Paulo., and S. Costanzo, *Recent Advances in Information Systems and Technologies: Volume 3*. Springer International Publishing, 2017, pp. 557.

[45] K. Gomez, S. Kandeepan, L. Reynaud, and T. Rasheed, "Adaptive energy efficient communications for rapidly deployable aerial-terrestrial networks," in *IEEE International Conference on Communications Workshops (ICC)*, 2013, pp. 452–457.

[46] S. Kandeepan, K. Gomez, T. Rasheed, and L. Reynaud, "Energy efficient cooperative strategies in hybrid aerial-terrestrial networks for emergencies," in *IEEE 22nd International Symposium on Personal, Indoor and Mobile Radio Communications*, 2011, pp. 294–299.

[47] 3rd Generation Partnership Project, "TR36.814 v9.0.0: Further advancements for E-UTRA physical layers aspects (release 9)," 3GPP, Sophia Antipolis, France, Tech. Rep., March 2010.

[48] F. Qixing, J. McGeehan, E. K. Tameh, and A. R. Nix, "Path loss models for air-to-ground radio channels in urban environments," in *IEEE 63rd Vehicular Technology Conference*, vol. 6, 2006, pp. 2901–2905.

[49] Q. Feng, E. K. Tameh, A. R. Nix, and J. McGeehan, "Modelling the likelihood of line-of-sight for air-to-ground radio propagation in urban environments," in *IEEE Globecom*, 2006, pp. 1–5.

[50] J. Holis and P. Pechac, "Elevation dependent shadowing model for mobile communications via high altitude platforms in built-up areas," *IEEE Transactions on Antennas and Propagation*, vol. 56, no. 4, pp. 1078–1084, 2008.

[51] C. A. Balanis, *Antenna Theory: Analysis and Design*. John Wiley & Sons, 2016.

[52] C. M. Grinstead and J. L. Snell, *Grinstead and Snell's introduction to probability*. Chance Project, 2006.

[53] Z. Gaspar and T. Tarnai, "Upper bound of density for packing of equal circles in special domains in the plane," *Periodica Polytechnica. Civil Engineering*, vol. 44, no. 1, p. 13, 2000.

Appendix: Derivation of PDF of Received Signal Strength

The probability density function of RSS at an arbitrary point in a cell is found by first deriving PDFs of LoS and NLoS component of RSS using transformations of RVs. Thereafter, Theorem 1 is applied.

From (3.13), the RV, S_l can be expressed as:

$$\begin{aligned} S_l &= P_l\, R_l \\ &= P_l \left[10 \log \left(\frac{29000}{B^2} \right) - 12 \left(\frac{\tan^{-1}\left(\frac{r}{h}\right) - \phi_{tilt}}{B} \right)^2 + T - 20\log\Big(\frac{4\pi f d}{c}\Big) \right] - P_l\, X_l \\ &= P_l\, A_1 - P_l\, X_l \end{aligned} \tag{9.1}$$

where P_l is given in (2.2) and A_1 can be treated as a constant for a UAV deployed at a fixed height and beamwidth, given by:

$$A_1 = T + 10 \log \left(\frac{29000}{B^2} \right) - 12 \left(\frac{\tan^{-1}\left(\frac{r}{h}\right) - \phi_{tilt}}{B} \right)^2 - 20\log\Big(\frac{4\pi f d}{c}\Big) \tag{9.2}$$

The derivation is proceeded by first finding PDF of S_l by applying transformations of random variables as follows:

$$\begin{aligned} F_{S_l}(s_l) &= \mathrm{P}\left(S_l \leq s_l\right) \\ &= \mathrm{P}\left(P_l\, A_1 - P_l\, X_l \leq s_l\right) \\ &= \mathrm{P}\left(X_l \leq \frac{s_l - P_l\, A_1}{P_l}\right) \\ F_{S_l}(s_l) &= F_{X_l}\left(\frac{s_l - P_l\, A_1}{P_l}\right) \end{aligned} \tag{9.3}$$

where $F_{S_l}(s_l)$ and $F_{X_l}(x_l)$ are the cumulative distribution functions (CDFs) of S_l and X_l respectively. Both sides of (9.3) are a function of s_l and therefore, we differentiate both sides w.r.t s_l in order to get the PDF:

$$f_{S_l}(s_l) = f_{X_l}\left(\frac{s_l - P_l\,A_1}{P_l}\right)\frac{d}{d\,s_l}\left(\frac{s_l - P_l\,A_1}{P_l}\right)$$
$$f_{S_l}(s_l) = \frac{1}{P_l} f_{X_l}\left(\frac{s_l - P_l\,A_1}{P_l}\right) \tag{9.4}$$

This allows to find the PDF of S_l based on the PDF of X_l which is $\mathcal{N}(0, \sigma_n)$ random variable. Applying the transformation in (9.4) yields the following expression for $f_{S_l}(s_l)$:

$$f_{S_l}(s_l) = \frac{\exp\left(-\frac{(s_l - P_l\,A_1)^2}{2(P_l\,\sigma_l)^2}\right)}{\sqrt{2\pi}P_l\,\sigma_l} \tag{9.5}$$

Following a similar procedure, we then derive PDF of S_n, which yields following expression:

$$f_{S_n}(s_n) = \frac{\exp\left(-\frac{(s_n - [P_n(A_1 - \mu_{sh})])^2}{2(P_n)^2\left(\sigma_n^2 + \sigma_{sh}^2\right)}\right)}{\sqrt{2\pi}P_n\sqrt{\sigma_n^2 + \sigma_{sh}^2}} \tag{9.6}$$

We can now proceed to apply Theorem 1 to derive PDF of S_r by performing convolution of (9.5) with (9.6) as in (9.7), where A_2 in (9.7) is expanded in (9.8).

$$\begin{aligned} f_{S_r}(s_r) &= \int_{-\infty}^{\infty} \frac{1}{\sqrt{2\pi}\,P_n\sqrt{\sigma_n^2 + \sigma_{sh}^2}} \exp\left[-\frac{(s_r - s_l - [P_n\,(A_1 - \mu_{sh})])^2}{2\,(P_n)^2\,(\sigma_n^2 + \sigma_{sh}^2)}\right] \frac{1}{\sqrt{2\pi}\,P_l\,\sigma_l} \exp\left[-\frac{(s_l - P_l\,A_1)^2}{2\,(P_l\,\sigma_l)^2}\right] d\,s_l \\ &= \int_{-\infty}^{\infty} \frac{1}{\sqrt{2\pi}\sqrt{2\pi}\,P_n\sqrt{\sigma_n^2 + \sigma_{sh}^2}\,P_l\,\sigma_l} \exp\left[-\frac{A_2}{2\,(P_l)^2\,\sigma_l^2\,(P_n)^2\,(\sigma_n^2 + \sigma_{sh}^2)}\right] d\,s_l \end{aligned} \tag{9.7}$$

$$\begin{aligned} A_2 &= (P_l)^2\,\sigma_l^2\,(s_r - s_l - [P_n\,(A_1 - \mu_{sh})])^2 + (P_n)^2\left(\sigma_n^2 + \sigma_{sh}^2\right)(s_l - P_l\,A_1)^2 \\ &= (P_l)^2\,\sigma_l^2\left(s_r^2 + s_l^2 + [P_n\,(A_1 - \mu_{sh})]^2 - 2s_l\,s_r - 2s_r\,[P_n\,(A_1 - \mu_{sh})] + \right. \\ &\qquad \left. 2s_l[P_l(A_1 - \mu_{sh})]\right) + (P_n)^2\left(\sigma_n^2 + \sigma_{sh}^2\right)\left(s_l^2 + (P_l\,A_1)^2 - 2s_l\,P_l\,A_1\right) \end{aligned} \tag{9.8}$$

Next, we perform algebraic manipulation on (9.8) in (9.9) to convert the terms in it to $(C + D)^2$ form in order to apply completing the squares method.

$$A_2 = s_l^2 \left[(P_l)^2 \sigma_l^2 + (P_n)^2 \left(\sigma_n^2 + \sigma_{sh}^2 \right) \right] - 2 s_l \Big[(P_l \sigma_l)^2 (s_r - P_n (A_1 - \mu_{sh})) + (P_n)^2 \left(\sigma_n^2 + \sigma_{sh}^2 \right) P_l A_1 \Big] + (P_l \sigma_l)^2 \left(s_r^2 + [P_n (A_1 - \mu_{sh})]^2 - 2 s_r [P_n (A_1 - \mu_{sh})] \right) + (P_n)^2 \left(\sigma_n^2 + \sigma_{sh}^2 \right) [P_l A_1]^2 \quad (9.9)$$

In order to complete the square of (9.9), we define a new variable in the following manner:

$$\sigma_s = \sqrt{\sigma_{s_l}^2 + \sigma_{s_n}^2} \quad (9.10)$$

where $\sigma_{s_l}^2 = (P_l \sigma_l)^2$ and $\sigma_{s_n}^2 = (P_n)^2 (\sigma_n^2 + \sigma_{sh}^2)$.

Therefore, the PDF expression in (9.7) reduces to:

$$f_{S_r}(s_r) = \int_{-\infty}^{\infty} \frac{1}{\sqrt{2\pi}\sigma_s} \frac{1}{\sqrt{2\pi}\frac{\sigma_{s_l}\,\sigma_{s_n}}{\sigma_s}} \exp \left[- \frac{A_3}{2(\frac{\sigma_{s_l}\,\sigma_{s_n}}{\sigma_s})^2} \right] \quad (9.11)$$

where A_3 equals to (9.12).

$$A_3 = s_l^2 - 2 s_l \frac{\sigma_{s_l}^2 (s_r - [P_n (A_1 - \mu_{sh})]) + \sigma_{s_n}^2 P_l A_1}{\sigma_s^2} + \frac{\sigma_{s_l}^2 (s_r^2 + [P_n (A_1 - \mu_{sh})]^2 - 2 s_r [P_n (A_1 - \mu_{sh})] + \sigma_{s_n} [P_l A_1]^2}{\sigma_s^2} \quad (9.12)$$

Squares are now completed by collecting the appropriate terms as in (9.13).

$$A_3 = \left(s_l - \frac{\sigma_{s_l}^2 (s_r - [P_n (A_1 - \mu_{sh})]) + \sigma_{s_n}^2 P_l A_1}{\sigma_s^2} \right)^2 - \left(\frac{\sigma_{s_l}^2 (s_r - [P_n (A_1 - \mu_{sh})]) + \sigma_{s_n}^2 P_l A_1}{\sigma_s^2} \right)^2 + \left(\frac{\sigma_{s_l}^2 (s_r - [P_n (A_1 - \mu_{sh})])^2 + \sigma_{s_n}^2 P_l^2 A_1^2}{\sigma_s^2} \right) \quad (9.13)$$

Finally, the exponent in (9.11) can be broken into a product of two exponents as shown in (9.14). By noting that the integral in (9.14) is in fact a Gaussian distribution on S_l (and hence integrates to 1), substituting σ_s from (9.10), P_l and P_n from (2.2) leads to the expression of PDF of S_r in (3.15).

$$f_{S_r}(s_r) = \frac{1}{\sqrt{2\pi\sigma_s}} \exp\left[-\frac{\left(s_r - [P_l\, A_1 + P_n\,(A_1 - \mu_{sh})]\right)^2}{2\sigma_s^2}\right] \underbrace{\int_{-\infty}^{\infty} \frac{1}{\sqrt{2\pi}\frac{\sigma_{s_l}\sigma_{s_n}}{\sigma_s}} \exp\left[-\frac{s_l - \frac{\sigma_{s_l}^2(s_r - [P_n(A_1 - \mu_{sh})]) + \sigma_{s_n}^2[P_l\, A_1]}{\sigma_s^2}}{2(\frac{\sigma_{s_l}\sigma_{s_n}}{\sigma_s})^2}\right] ds_l}_{=1} \quad (9.14)$$